Univ.-Prof. Dr. Friedrich Aumayr

DIPLOMARBEIT

Experimental and Simulated Sputtering of Gold, Iron and Wollastonite with a Catcher-QCM Setup

Ausgeführt am Institut für
Angewandte Physik der
Technischen Universität Wien
Wiedner Hauptstraße 8-10 / 134
1040 Wien

unter der Anleitung von
Univ.-Prof. Dr. Friedrich Aumayr
und
Dr. Bernhard M. Berger
durch

Paul Stefan Szabo
Matrikelnummer: 01225017
Breitenseer Straße 58/9
1140 Wien

Wien, am 4. September 2017 Paul Szabo

Abstract

When ions of the solar wind hit rocky bodies such as the Moon or Mercury they have a major effect on the surface of these bodies in a process called space weathering. Furthermore, sputtered material forms a thin exosphere that can be investigated in order to gain information about the body's surface. A detailed understanding of the underlying physical processes can give important insights into planets, moons and asteroids.

Establishing experimental data for these effects is a very important improvement for research on space weathering and exosphere formation. This thesis describes both experimental and theoretical investigations of sputtering measurements of various targets with a setup where a quartz crystal microbalance (QCM) is used as a catcher to collect sputtered material. These targets include Au for testing purposes, Fe for investigating surface roughness effects and Wollastonite ($CaSiO_3$), which represents a moon analogue material for investigating sputtering by solar-wind ions.

In Section 1, the motivation will be presented along with a background on the sputtering effects relevant for this thesis. Section 2 then describes the QCM technique for measuring sputtering yields as well as the catcher-QCM setup, which allows indirect sputtering measurements. Furthermore, an overview of the sample preparations and analysis techniques that were performed is given. The theoretical approach for simulating catcher-QCM measurements and the software used are presented in Section 3, along with a description of simulating rough surfaces with SDTrimSP-2D. Finally, Section 4 presents experimental results along with a comparison to simulation results and discusses how the differences in them can be explained. The conclusion in Section 5 gives a summary of the knowledge gained through this thesis and describes how the catcher-QCM setup might be improved in the future.

Both experiments and simulations show a very good agreement over a wide variety of parameters for all investigated samples. Showing the feasibility of the catcher setup opens up several possibilities for more realistic measurements of the solar-wind sputtering using rock or powder targets. The coinciding results of the experiments also indicate that the particle distributions of the sputtered materials provided by SDTrimSP can very confidently be used for simulating exosphere formations.

Kurzfassung

Sonnenwind-Ionen, die auf die Oberfläche von Gesteinskörpern wie Mond oder Merkur treffen, verursachen eine starke Veränderung dieser Oberflächen durch einen Prozess, der als Weltraumverwitterung bezeichnet wird. Außerdem bildet sich eine dünne Exosphäre aus zerstäubtem Material, welches untersucht werden kann, um Rückschlüsse auf die Oberflächenzusammensetzung des betrachteten Planeten, Mondes oder Asteroiden zu ziehen. Ein genaues Verständnis der zugrunde liegenden physikalischen Prozesse kann dabei einen wichtigen Beitrag zur Erforschung dieser Objekte leisten und die Ermittlung experimenteller Daten, die diese Effekte beschreiben, stellt eine bedeutende Verbesserung für die Forschung im Bereich der Weltraumverwitterung und der Exosphären-Bildung dar.

Die vorliegende Arbeit beschäftigt sich sowohl experimentell als auch theoretisch mit der Untersuchung des Zerstäubungsverhaltens verschiedener Materialien. Dabei kommt ein experimenteller Aufbau zum Einsatz, beim dem eine Quarzkristall-Mikrowaage (QCM) als Auffänger für zerstäubtes Material verwendet wird. Die untersuchten Proben sind Au, um den Aufbau zu testen, Fe, um den Einfluss verschiedener Oberflächenrauigkeiten zu untersuchen, und Wollastonit, ein Mond-Analogmaterial, das sich für erste realistische Untersuchungen des Zerstäubens durch Sonnenwind-Ionen eignet.

In Kapitel 1 werden die Motivation für diese Arbeit und eine Zusammenfassung der für die durchgeführten Experimente relevanten Zerstäubungseffekte präsentiert und in Kapitel 2 werden die QCM-Methode zur Messung von Zerstäubungsausbeuten und der Auffängeraufbau, der eine indirekte Untersuchung der Zerstäubung ermöglicht, beschrieben. Außerdem wird ein Überblick über die verwendeten Techniken zur Probenpräparation und -analyse gegeben. Die Simulation der Auffänger-QCM-Messungen und die dafür verwendeten Computer-Programme werden in Kapitel 3 behandelt, das auch eine Beschreibung der Simulationen rauer Oberflächen mit dem Programm SDTrimSP-2D beinhaltet. Die Resultate der Messungen werden schließlich in Kapitel 4 präsentiert und mit den Ergebnissen der Berechnungen verglichen. Das Fazit in Kapitel 5 fasst die in der vorliegenden Arbeit gewonnenen Erkenntnisse zusammen und erläutert, wie der Auffängeraufbau in Zukunft verbessert werden kann.

Die experimentellen und die theoretischen Resultate stimmen bei allen verwendeten Proben und einem Großteil der untersuchten Parameter sehr gut überein.

Diese vielversprechenden Ergebnisse mit dem neuen Aufbau eröffnen damit neue Möglichkeiten für realistischere Untersuchungen der Zerstäubung durch Sonnenwind-Ionen, zum Beispiel mit Stein- oder Pulverproben. Die mit SDTrimSP berechneten Teilchen-Verteilungen des zerstäubten Materials, mit denen sich die experimentellen Resultate verlässlich reproduzieren lassen, sind daher auch geeignet, die Bildung von Exosphären zu simulieren.

List of Publications

Publications in Scientific Journals

- B. M. Berger, **P. S. Szabo**, R. Stadlmayr, F. Aumayr: *Sputtering measurements using a quartz crystal microbalance as a catcher*, Nucl. Instrum. Meth. Phys. Res. B 406 (2017), 533-537.

Contributions to International Conferences

Short Oral Presentation

- **P. S. Szabo**, R. Chiba, B. M. Berger, R. Stadlmayr, H. Biber, M. Doppler, J. Appenroth, A. Galli, M. Sauer, H. Hutter, J. Fleig, P. Wurz, F. Aumayr: *Sputtering of Wollastonite*, 22nd International Workshop on Inelastic Ion-Surface Collisions (IISC 22), September 17th-22nd, 2017.

Posters

- **P. S. Szabo**, B. M. Berger, R. Stadlmayr, F. Aumayr: *Sputtering Measurements with a New Catcher QCM Setup*, 27th International Conference on Atomic Collisions in Solids (ICACS-27), July 24th-29th, 2016.

- **P. S. Szabo**, B. M. Berger, R. Stadlmayr, A. Galli, H. Lammer, P. Wurz, F. Aumayr: *A new setup for sputtering experiments with Mercury and Moon analogues*, 12th European Conference on Atoms, Molecules and Photons (ECAMP 12), September 5th-9th, 2016.

- **P. S. Szabo**, B. M. Berger, R. Chiba, R. Stadlmayr, F. Aumayr: *A new setup for experimental investigations of solar wind sputtering*, European Geosciences Union General Assembly 2017 (EGU 2017), April 23rd-28th, 2017.

Contents

Abstract i

Kurzfassung ii

List of Publications iv

Contents v

1 Introduction 1
- 1.1 Motivation 1
- 1.2 Sputtering by Ion Bombardment 6
  - 1.2.1 Different Sputtering Effects 6
  - 1.2.2 Sputtering Yield Y 8
  - 1.2.3 Particle Distributions 10
  - 1.2.4 Sputtering of Rough Surfaces 14
- 1.3 Outline 16

2 Experimental Methods 17
- 2.1 AUGUSTIN Ion-Beam Facility 17
- 2.2 Quartz Crystal Microbalance (QCM) 19
  - 2.2.1 Measuring Sputter Yields with a QCM 19
- 2.3 Catcher-QCM Setup 24
  - 2.3.1 Design 24
  - 2.3.2 Evaluation Methods 26
  - 2.3.3 The parameter g 28
- 2.4 Sample Preparation and Analysis 29
  - 2.4.1 Au QCM-Films 29
  - 2.4.2 Fe QCM-Films 30
  - 2.4.3 Wollastonite ($CaSiO_3$) 34

3 Theoretical Description of Catcher Measurements 42
- 3.1 Calculating y_C 42
  - 3.1.1 Contribution of Sputtered Atoms 42
  - 3.1.2 Contribution of Reflected Ions 45
  - 3.1.3 Conclusion 46

3.2 SDTrimSP Simulations 47
  3.2.1 Detailed calculation of $y^j_{\mathrm{C,r}}$ and $y^i_{\mathrm{C,sp}}$ 48
  3.2.2 Summary 52
3.3 Simulation of Rough Surfaces with SDTrimSP-2D 54
  3.3.1 SDTrimSP-2D 54
  3.3.2 Approach for Fe Simulations 55

4 Results and Discussion **57**
4.1 2 keV Ar^+ on Au 57
4.2 1 keV Ar^+ on Fe 61
  4.2.1 Target Sputtering Yield 62
  4.2.2 Catcher Measurements 64
4.3 2 keV Ar^+ on Wollastonite ($\mathrm{CaSiO_3}$) 68
  4.3.1 Target Mass Removal Rate 68
  4.3.2 Catcher Measurements 70

5 Conclusion and Outlook **74**

References **77**

List of Figures **85**

List of Tables **85**

List of Abbreviations **86**

Danksagung **87**

1 Introduction

1.1 Motivation

Space weathering is a very important aspect for planetary science. It describes the erosion and transformation of the surfaces of rocky bodies in the solar system as a result of different influences from space [1]. Generally, these asteroids, moons or planets are exposed to the impact of meteroites, electromagnetic radiation and ions ([2], [3]). With regard to the lunar surface, the consequences of meteorite impacts are apparent, as its surface is covered by craters. However, observed darkening processes of these craters' surroundings lead to the assumption that there are also interactions taking place that change the optical properties of the lunar soil [4]. This was experimentally verified after the first NASA Apollo missions, where lunar material turned out to be darker than comparable pulverized stones [5]. What was first thought to be caused by vitrification processes [6], where glass particles are created as a result of meteorite impacts, was then attributed to ion sputtering and impact vaporization ([7], [8]). It was found that a darkening of powder samples is created from "submicroscopic metallic iron" that forms coherent crusts on the powder [1].

Besides an optical change of the surface, particles are evaporated and a tenuous atmosphere, an exosphere, is created. This exosphere is interesting for planetary science as its composition allows conclusions on the composition of the planetary surface [9]. It thus enables another method of remotely investigating objects in the solar system besides spectroscopically examining characteristic absorption lines [10]. During flyby missions, this exosphere can be analyzed and as a result, information on the surface can be gained without having the complex task of landing a spacecraft. Several such missions have been performed in the past, for example the Messenger mission to Mercury [11], and in the Bepi Colombo mission another spacecraft is planned which has the goal of analyzing the Mercury exosphere [12].

The main release processes for creating exospheres are identified as thermal desorption, photon-stimulated desorption by UV light, impact vaporization due to micrometeorites and sputtering by ions from the solar wind or magnetospheric plasmas [13], as is indicated in the sketch in Figure 1. For volatile species (elements with a high vapor pressure) mainly desorption processes ([2], [14]) and impact vaporizations ([3], [15]) are important. In the lunar exosphere Ar and He were found [16], while

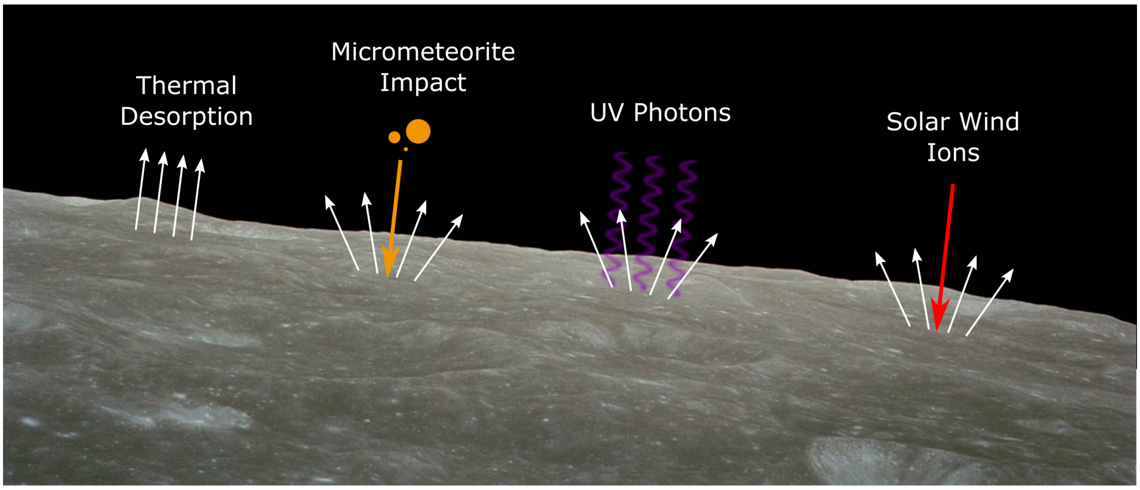

Figure 1: This image shows the different processes that are responsible for space weathering: Desorption from the surface due to thermal energy, surface erosion due to micrometeorites hitting the surface, photon-stimulated desorption by UV light and sputtering of atoms by solar-wind ions.

the volatile part of Mercury's exosphere is dominated by H, He, O, Na and K [17]. On the other hand, the erosion of refractory species, which make up a large part of a planet's or moon's mass by forming rocks, is dominated by impact vaporization and ion sputtering [9], with Ca and Mg dominating at Mercury [17].

On the Moon, sputtering is mostly caused by solar-wind ions. The solar wind is a plasma stream that escapes the solar corona due to its high temperature and the Sun's magnetic field [18]. It is generally said to consist of two elements: fast ions at speeds of more than 750 km/s at high heliographic lattitudes, and slower ions at 450 km/s at lower lattitudes [19]. The solar wind's composition is dominated by H (protons) with small parts of He and highly charged heavier ions (see Table 1). Even though they only make up a minor part of the solar wind, the latter are important for considering the sputtering effects of the solar wind. Figure 2 shows a solar-wind ion spectrum over energy per charge state E/q. H and He mostly occur at energies between 1 and 10 keV, while heavier ions are able to reach significantly higher kinetic energies and will have higher sputtering yields. Additionally, on insulating materials their sputtering yield is further enhanced by potential sputtering (see the following section 1.2) due to their high charge states.

Element	**Relative Concentration**	**Charge States**
H	1	1^+
He	0.07	2^+
C	$5 \cdot 10^{-4}$	$4^+ - 6^+$
N	$5 \cdot 10^{-5}$	$5^+ - 7^+$
O	$7 \cdot 10^{-4}$	$5^+ - 8^+$
Ne	$9 \cdot 10^{-5}$	$7^+ - 9^+$
Mg	$1 \cdot 10^{-4}$	$7^+ - 10^+$
Si	$1 \cdot 10^{-4}$	$6^+ - 12^+$
S	$3 \cdot 10^{-5}$	$6^+ - 11^+$
Ar	$2 \cdot 10^{-6}$	$7^+ - 10^+$
Fe	$8 \cdot 10^{-4}$	$7^+ - 14^+$

Table 1: This table gives an overview of the composition of the solar wind. It shows the concentration relative to H and the charge states for the most prominent species. As it can be seen clearly, H and He make up the largest part of the solar wind, while heavier, highly charged ions have a lower concentration, but their high kinetic and potential energy can still considerably contribute to sputtering. (Data taken from ([20], [21])).

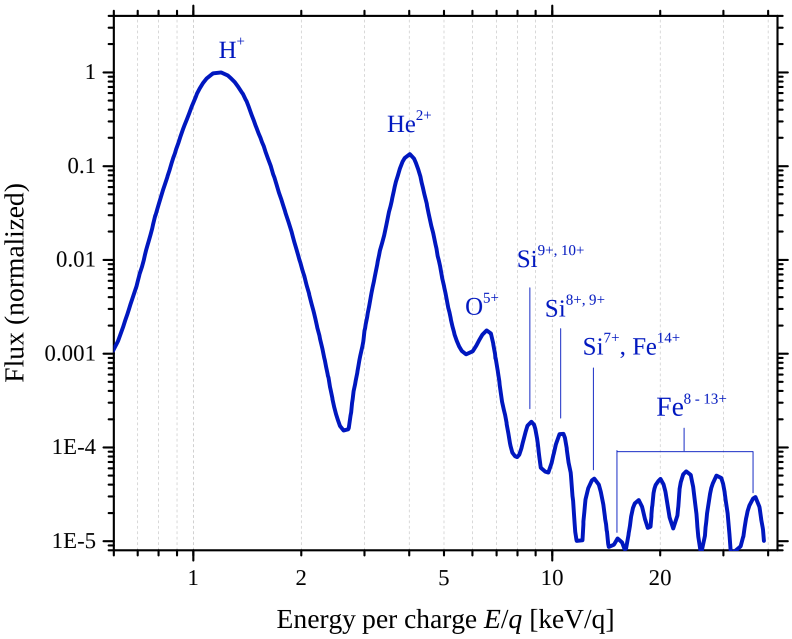

Figure 2: This graph shows a spectrum of solar-wind ions, where the normalized ion flux is plotted logarithmically over the energy/charge state ratio E/q. It shows clearly that the solar wind is dominated by protons of around 1 keV, while the rarer heavier ions can reach over 10-100 keV (>10 keV/q). This kinetic energy and their high charge states q lead to increased sputtering yields, which is why they also have to be taken into account for space weathering. (Taken from [21] and [22].)

On a planet like Mercury, a different situation is found. Mercury has not been able to retain an atmosphere that would sufficiently shield it against ion bombardment [23], but solar-wind ions predominantly hit the polar regions, where they are not deflected by the planet's magnetic field [24]. However, there is a contribution by a plasma precipitation from Mercury's magnetosphere on its nightside [25].

Taking all the effects that can cause space weathering into account, simulations can be performed to calculate exosphere densities, as it is done for the Moon [26] and Mercury [27]. The input for the sputtering contribution is taken from SRIM simulations [28], as there have not yet been many experimental investigations of the sputtering of relevant analogue materials (see [20] for an example). As a result, performing such experiments and examining how well the sputtering behavior of lunar or planetary rocks can be described with existing simulations such as TRIM or SDTrimSP could bring a substantial improvement for modelling space weathering effects. Furthermore, a more precise investigation of the potential sputtering effects by highly charged solar-wind ions will provide important insights, as they are often overlooked in simulations.

The main goal of this thesis is to take a first step into using the existing knowledge of the Institute of Applied Physics (IAP) about ion-surface interactions and sputtering in particular to investigate the sputtering contribution to space weathering. Sputtering experiments at IAP have been performed for several decades using a Quartz Crystal Microbalance (QCM) technique for measuring sputtering yields [29], which will be presented in Section 2.2. By measuring the frequency change of an oscillating quartz it allows precise in-situ measurements of a thin film's mass change due to sputtering. Using a QCM, effects like potential sputtering ([30], [31]) or the erosion of potential wall materials for a nuclear fusion reactor have been investigated ([32], [33], [34]). Recently, a new experimental setup was developed that allows using a QCM as a catcher for sputtered atoms and thus enables measurements on a wide range of targets [35]. First experimental work using this catcher setup is presented in this thesis, including measurements with Au and Fe targets as well as the first astrophysically relevant investigations of the sputtering of Wollastonite ($CaSiO_3$), which can be found in lunar regolith [36].

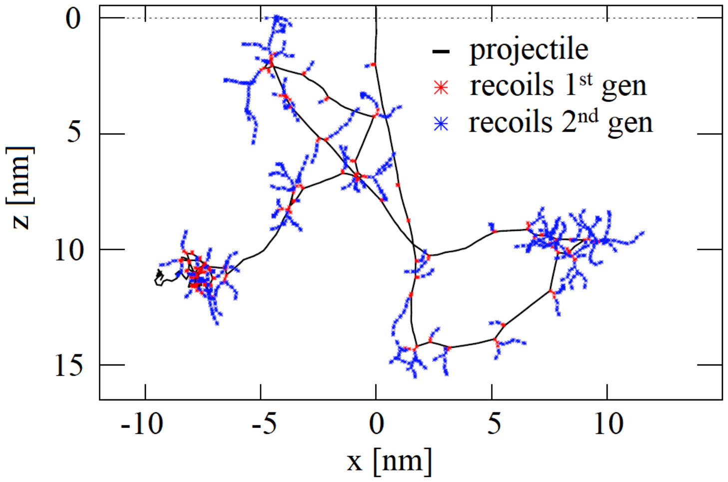

Figure 3: This picture shows the simulated trajectories of a 2 keV He atom entering a Ni target. The path of the projectile is denoted by the black line, while red and blue dots show recoils of the first and second generation respectively. In this example, it takes several collisions before a target atom has the right momentum to be sputtered. The trajectories shown in this image are from SDTrimSP simulations, with the picture being taken from [38].

1.2 Sputtering by Ion Bombardment

Sputtering denotes the erosion of a solid's surface by the bombardment by ions with energies from eV to MeV [37]. A target atom will be sputtered if its kinetic energy in a direction normal to the surface exceeds the surface binding energy. Different origins for sputtering can be found depending on the target-projectile combination.

1.2.1 Different Sputtering Effects

Kinetic Sputtering Kinetic sputtering can be described as a series of interatomic collisions and was explained theoretically by Sigmund in 1969 [39]. An ion that enters a solid can only move a certain distance before it is scattered at a target atom and transfers some of its kinetic energy to the atom. Several such collisions as well as collisions between recoils and other target atoms lead to a cascade, with a simulated example being shown in Figure 3. As can be seen in this picture, sputtering of a target atom only happens after several collisions have taken place. Only then the projectile can pass on enough momentum onto a target atom to overcome the surface

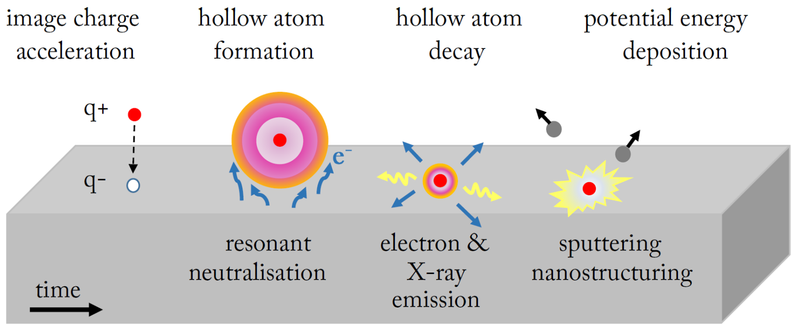

Figure 4: This diagram gives an overview of the interaction processes, when a highly-charged ion (HCI) hits a surface. First, the ion's image charge leads to an additional acceleration towards the surface. Processes of electron exchange then lead to the formation of a highly-excited hollow atom. After emitting some of its potential energy as electrons and photons, it deposits the remaining energy in the surface. This leads to target atoms being sputtered, which is denoted as potential sputtering, and other effects such as nanostructuring. Image taken from [40].

binding energy. For this reason, there is a threshold energy for kinetic sputtering, which is in the range of 10 - 100 eV [37].

Potential Sputtering For slow highly-charged ions (HCI), one also has to take into account the ions' potential energy, which may lead to an increased sputtering yield for semiconducting and insulating target materials [31]. The interaction between such an HCI and the target surface already starts before the ion hits the surface, as is sketched in Figure 4 [40]. After being further accelerated by its image charge, electron exchange processes lead to a partial neutralization of the projectile ions via resonant neutralization. Electrons overcome the potential barrier between target and ion and occupy highly-excited Rydberg states, while the inner more tightly bound states are left empty. This leads to the formation of a so-called hollow atom [41], which decays over a wide variety of processes, where electrons and X-ray photons are emitted. However, the ion still retains some of its potential energy, which is finally transfered into a small volume of the target. There nanostructuring has been found to occur ([42], [43]), as well as further sputtering due to the ion's potential energy [31].

Preferential Sputtering Sputtering yields are strongly dependent on the target-projectile combination, and for this reason different species in compound materials are sputtered at varying rates. This preferential sputtering causes an alteration of the surface composition, thus fluence dependence finally leads to a steady state behavior. There differences in sputtering yields and concentration cancel each other and the mass removal rate by ion sputtering becomes stable.

Chemical Sputtering, Channeling Further effects that influence the sputtering behavior have been found: chemical sputtering can occur when reactions between target and projectile material can change the surface binding energy and thus influence the sputtering behavior [44]. This can lead to an increase as well as a decrease in the sputtering yield. Ion bombardment of a crystalline target is influenced by the crystal orientation, with channeling effects causing lower sputtering yields [45].

1.2.2 Sputtering Yield Y

The key quantity to describe sputtering effects is the sputtering yield Y, which is defined as

$$Y = \frac{\text{number of sputtered target atoms}}{\text{number of incident ions}}$$

For the experiments in this thesis, it is mostly kinetic sputtering that has to be taken into account. Then Y is dependent on the projectile's mass, the target's mass, the projectile's kinetic energy and the angle of incidence. Variations in these parameters have been investigated experimentally and theoretically in recent decades with a large database being already available. The following pictures (Figure 5 and 6) give examples of the general behaviors that have been found.

First, Figure 5 depicts experimentally determined sputtering yields under variation of impact energy and angle. The graph on the left (taken from [37], data from the references therein) shows experimental and calculated sputtering yields for Ar ions hitting a Fe sample under normal incidence for different energies. The logarithmic plot shows a threshold energy of 10-20 eV with a strong increase for low energies as more energy is available to be passed on to target atoms. For keV energy ranges, under which most experiments at IAP are performed, the sputtering yield here is in the order of 1, its maximum of ≈ 3 can be found at energies of about 10 keV. Ions

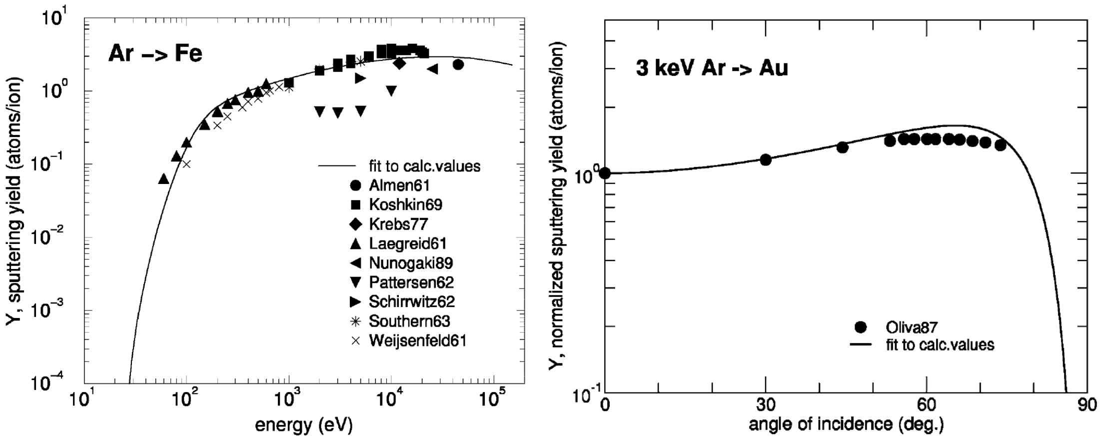

Figure 5: The graph on the left shows measured and calculated sputtering yields at different energies for Fe bombardment with Ar ions under normal incidence. Above the threshold energy, the sputtering yield increases as more energy is available to be transfered in a collision cascade. However, there is a maximum for Y, after which the interaction cross-section decreases, which results in lower sputtering yields.

The right-hand graph shows the same plots for an Au target and 3 keV Ar projectiles at different projectile angles of incidence, with the sputtering yield being normalized to its value at 0 degrees. Oblique incidence results in an increased sputtering yield as the collision cascade takes place closer to the surface. For large angles of incidence, however, the reflection of ions at the surface becomes more important, which results in fewer atoms being sputtered.

Both images are taken from [37], for the experimental data see the references give in [37].

faster than that experience a decrease in the nuclear interaction cross-section and thus a lower stopping power, which results in a decreasing sputtering yield [39].

The right-hand graph in Figure 5 shows the dependency of the normalized sputtering yield $Y(\alpha)/Y(0^\circ)$ on the angle of incidence α with 0 degrees being denoted as normal incidence. It shows an increased sputtering yield for oblique incidence with a maximum that is usually found at about 60 degrees. The increase can be explained by two aspects: Firstly, as Figure 3 shows, several collisions are necessary to result in a sputtered atom, as the momentum perpendicular to the surface has to be transversed. This becomes easier for larger angles of incidence because in this case the ions have less initial momentum in the direction normal to the surface. Furthermore, the collision cascade created by the projectile ion is moved closer to the surface due to the skew incidence and thus more atoms can be sputtered. Under grazing incidence more and more ions are reflected from the surface and as a result, the sputter yield decreases again.

1.2.3 Particle Distributions

For more detailed experimental research of sputtering effects, as intended with the catcher-QCM setup at IAP, the sputtering yield Y does not represent the only quantity of interest. Knowledge about energy and angular distributions both for sputtered target atoms and reflected projectile ions are also required.

First, Figure 6 gives examples for the energy distributions of sputtered and reflected particles. The graph on the left shows a comparison between measured intensities of sputtered Ca atoms and a calculation [37] for 4 keV Ar^+ bombardment under normal incidence. This demonstrates an excellent agreement, where the vast majority of sputtered atoms is shown to be emitted below 10 eV. This fact becomes important for the description of the catcher setup (see section 2.3) as the energy of the sputtered atoms is below the sputtering threshold [46]. Sputtered atoms originating from the target that hit the catcher-QCM will thus not cause any sputtering there, which simplifies the simulation of the catcher measurements. For reflected ions, the situation is very different, as is shown in the right-hand graph in Figure 6. It depicts the energy of reflected ions taken from an SDTrimSP simulation of 2 keV Ar^+ ions hitting a Au surface under an angle of incidence of 60 degrees. While there are some ions below the threshold, the rest are reflected with energies ranging nearly up to the initial 2000 eV. The fact that the number of reflected ions reaches 0

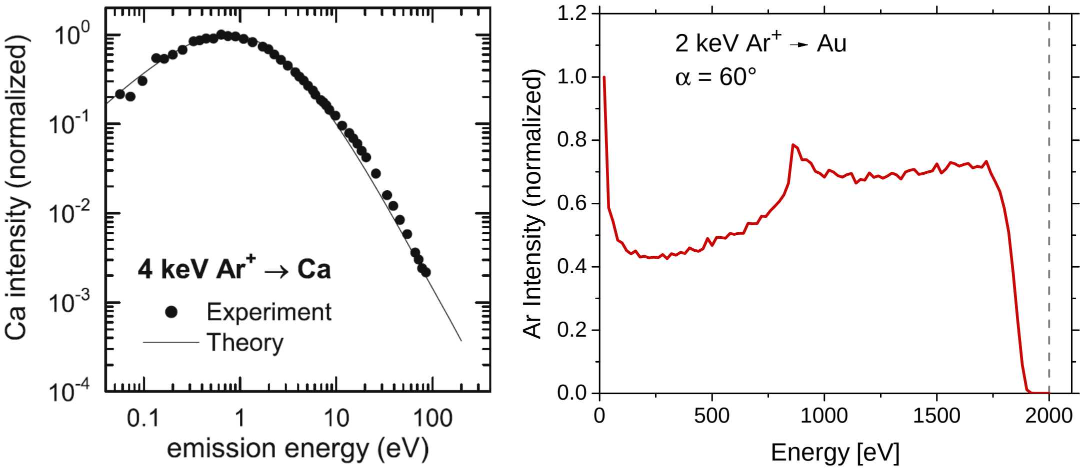

Figure 6: The graph on the left shows the energy distribution for sputtered target atoms after the bombardment of a Ca target with 4 keV Ar^+ ions under normal incidence, normalized to the maximum intensity. Most sputtered particles have energies below 10 eV, which is below the sputtering threshold [46]. (Picture taken from [37].)

The right-hand graph shows the simulated energy distribution of reflected projectiles for 2 keV Ar^+ bombardment of a Au target under an angle of incidence of 60 degrees, normalized to the maximum intensity. In contrast to before, it shows a distribution over a wide range of energy nearly up to the initial energy of 2 keV. The maximum energy of about 1800 eV can be explained by the fact that each reflected ion undergoes at least one collision where it loses some of its energy to a target atom.

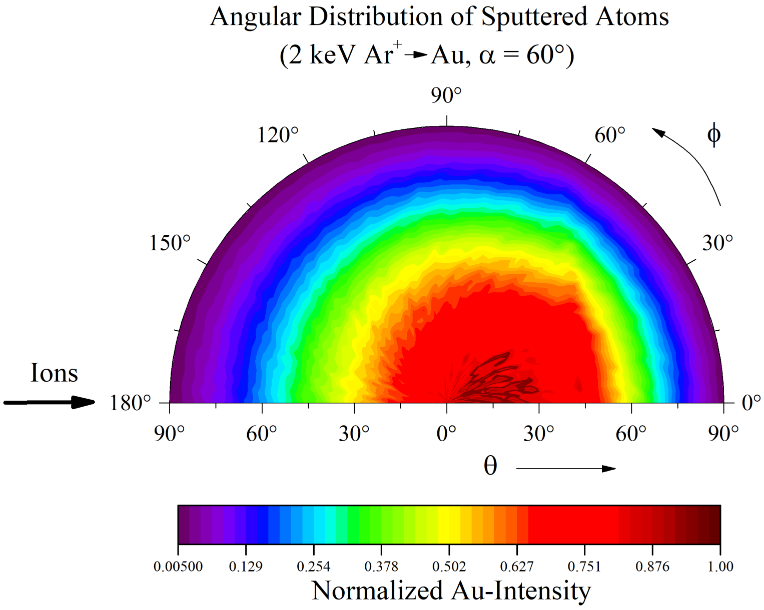

Figure 7: This image shows a simulated normalized angular distribution of sputtered atoms for the bombardment of a Au target with 2 keV Ar^+ ions under 60 degrees, with the ions arriving horizontally from the left in the plot. The distribution of sputtered atoms shows only very little azimuthal anisotropy with a small shift along the direction of the incoming ions. Similar as for normal incidence, the atoms are still concentrated in areas of low polar angles θ.

below 2 keV can be explained by the fact that each reflected projectile collides with at least one surface atom and so it is impossible for it to retain all of its energy.

The angular distribution of sputtered target atoms and reflected projectile ions are very important for the geometry of a sputtering experiment. On the one hand, catcher-QCM measurements rely on a precise knowledge of these distributions in order to interpret the measurements. Additionally, they also influence sputtering of rough surfaces, where redeposition of sputtered material and multiple sputtering by reflected ions are strongly dependent on the angular distributions. Figures 7 and 8 show simulated examples of these quantities for the bombardment of a Au target with 2 keV Ar^+ ions under an angle of 60 degrees. The distribution for sputtered particles for normal incidence can roughly be approximated with a $\cos\theta$ distribution, while a $(\cos\theta)^y$ with $1 < y < 2$ usually provides a good fit function [37]. Figure 7 shows a similarity to this cosine distribution, but a small shift in the direction of the incoming ions can be observed due to the high initial momentum parallel to the

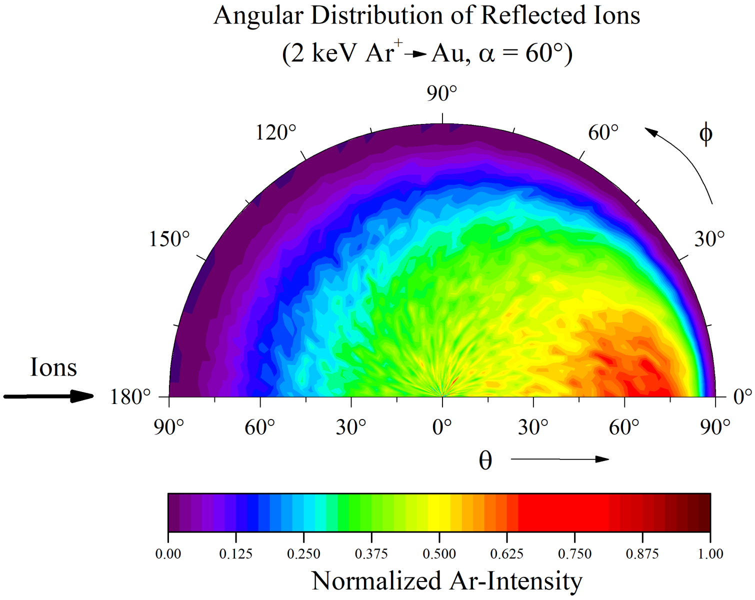

Figure 8: This image shows the normalized angular distribution of reflected ions for the same simulation as in Figure 7. The distribution of reflected ions looks very different, with the center of the distribution being found around the direction that corresponds to a classical reflection on a flat surface. Hereby, ions with higher energies tend to be concentrated around this direction, while ions with smaller energies that take part in multiple collisions before being reflected are found to be reflected without a preferential azimuthal angle.

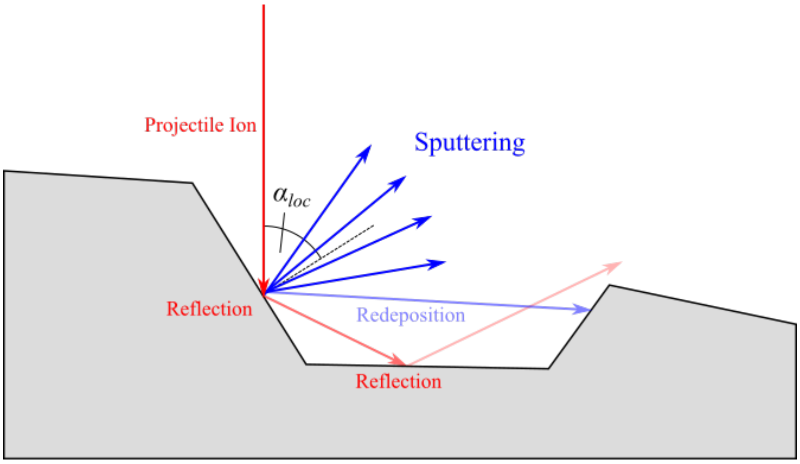

Figure 9: This sketch gives an overview of sputtering on a rough surface. A projectile ion, which is represented by the red arrow, hits a surface under nominal normal incidence. The local angle of incidence α_{loc} differs, however, due to the surface structure and thus affects the sputtering yield. Some of the sputtered atoms cannot escape the surface and get redeposited, while multiple reflections of the incidence ion lead to further erosion of the surface.

surface. Further anisotropic aspects are supressed by the process of several collisions being necessary to result in a sputtered atom.

However, such considerations do not hold for reflected ions, which show a much more pronounced shift in their distribution, which is presented in Figure 8. The highest concentration can be found roughly around the direction with $(\theta, \phi) = (60°, 0°)$, which corresponds to a classical reflection. Ions with energies close to the initial impact energy can be found preferentially concentrated around this direction. On the other hand, ions that go through several collisions in the target before escaping with low kinetic energies are found to have a less pronounced azimuthal asymmetry. As can be seen, a small number of ions are even reflected in the direction of incoming projectile ions.

1.2.4 Sputtering of Rough Surfaces

Theoretical descriptions (see [39]) and simulations (see [38]) of sputtering often only take into account flat surfaces. However, this is an idealization, and while it is possible to create reasonably flat films for some materials, this assumption will lead to discrepancies with experimental conditions. Figure 9 shows a sketch of how the roughness of a surface affects the sputtering. It shows a projectile ion (red arrow) hitting the surface under a nominal angle of 0 degrees, which would mean normal incidence for a perfectly flat surface. However, due to the surface structure the local angle of incidence α_{loc} is different, with its value being strongly dependent on the exact point of incidence. There the two already discussed events of surface sputtering and ion reflection occur. On average $Y(\alpha_{\mathrm{loc}})$ atoms are sputtered preferentially in the direction of the local surface normal. As is indicated in Figure 9, not all of the sputtered atoms are able to escape the surface. Some of them hit the right flank and are deposited there, which can be described by a redeposition factor R. Additionally, the ion is reflected with a probability of $P_r(\alpha_{\mathrm{loc}})$ and may hit the surface a second time. As it was discussed in Figure 6, the reflected ion's energy is lower than the incident energy, but still high enough to lead to further sputtering. These sputtered particles are then again partly redeposited and with a given probability further reflection may occur, whose depiction is omitted in Figure 9 for comprehensibility purposes.

Ultimately, the sputtering yield Y for a rough surface is given as a sum of all these effects:

$$Y = \sum_n P_r^n \cdot Y(E^{(n)}, \alpha_{\mathrm{loc}}^{(n)}) \cdot (1 - R^{(n)}) \tag{1}$$

with P_r^n signifying the probability of the nth reflection, $E^{(n)}$ describing the ion's energy after n reflections, $\alpha_{\mathrm{loc}}^{(n)}$ describing its local angle of incidence and $R^{(n)}$ the respective redeposition factor.

Evidently, a theoretical description of the sputtering of rough surfaces becomes quite complex. Küstner et al. achieved remarkable results using STM images as an input and a simple model to describe redeposition effects ([47], [48]). However, more detailed modeling of this situation is necessary to take into account effects such as shadowing (especially for flat ion incidence, some parts of the surface will not be hit by ions) and the change in angular and energy distributions, where Figure 9 already indicates large changes compared to a flat surface. For this reason, the investigations of rough Fe surfaces which are included in this thesis are simulated with the newly developed SDTrimSP-2D code ([49], [50]), which makes it possible to take surface structures into account in the sputtering calculations (see Section 3.3 for more information on the simulation and Section 4.2 for the presentation of the results).

1.3 Outline

In this section, the motivation and the physical effects that are relevant for this thesis were introduced. Following up, Section 2 will present the experimental methods that were used with an emphasis on the QCM technique, which allows precise in-situ sputtering measurements, and the catcher-QCM setup, which enables unique possibilities for using a wide variety of targets. Using this catcher-QCM setup to collect sputtered material requires a theoretical model for calculating sputtering yields of the initial target. It takes into account the geometry of the setup and the distributions of sputtered atoms and reflected ions to reproduce the measured signal, which is described in detail in Section 3. Section 4 then shows the results of both experiments and simulations for different targets discussing both concurrence and disparities between these results. Solving these problems and performing further experiments remain challenges for future work in this field, which will be highlighted in Section 5.

2 Experimental Methods

The experiments shown in this thesis are performed at the Augustin ion-beam facility at the IAP at TU Wien. An overview of this experimental setup is given at the beginning of this section followed by an explanation of the Quartz Crystal Microbalance (QCM) technique, which allows high-precision in-situ measurements of the sputtering yield. The QCM is used as part of a catcher setup for measuring the sputtering yield of a wide variety of targets, which will be presented thereafter. At the end of this section, the different samples investigated and the necessary methods of sample preparation and analysis are shown.

2.1 Augustin Ion-Beam Facility

An overview of the Augustin ion-beam facility is given in Figure 10. It is built around a 14.5 GHz Electron Cyclotron Resonance Ion Source (ECRIS) which was developed to optimize experiments with slow multiply-charged ions ([51], [52]). In such an ECRIS, a plasma is confined magnetically and heated with microwave radiation. Gas atoms are then ionized due to electron cyclotron resonance and can be extracted by a voltage of up to several kV to form the ion beam. This beam is then focused by a lens system consisting of two sets of quadrupole magnets and deflected into one of the experiment's three beamlines by a sector magnet (indicated by the red arrows in Figure 10). Its magnetic field is also used as a selector for the desired mass over charge state ratio of the beam's ions.

The experimental setup described in this thesis is connected to the beamline that is represented by the full red arrow in Figure 10. There the ion beam can be guided and formed by two sets of electrostatic deflection plates and an einzel lens. Using this setup the ion beam is focused into the sample chamber, where a pair of scanning plates is used to create a uniform current profile across the sample. This is achieved by applying alternating voltages to these plates with a frequency of 1.6 kHz and 52 Hz respectively so that the focused ion beam is scanned over a specified area. Inside the sample chamber, a target holder and a catcher-QCM are mounted on manipulators, which will be presented in detail in Section 2.3.

The Augustin ion-beam facility operates under Ultra-High Vacuum (UHV) conditions, which is maintained by membrane, turbomolecular and ion pumps. Pressures as low as 10^{-10} mbar enable ion-beam and surface experiments with minimal

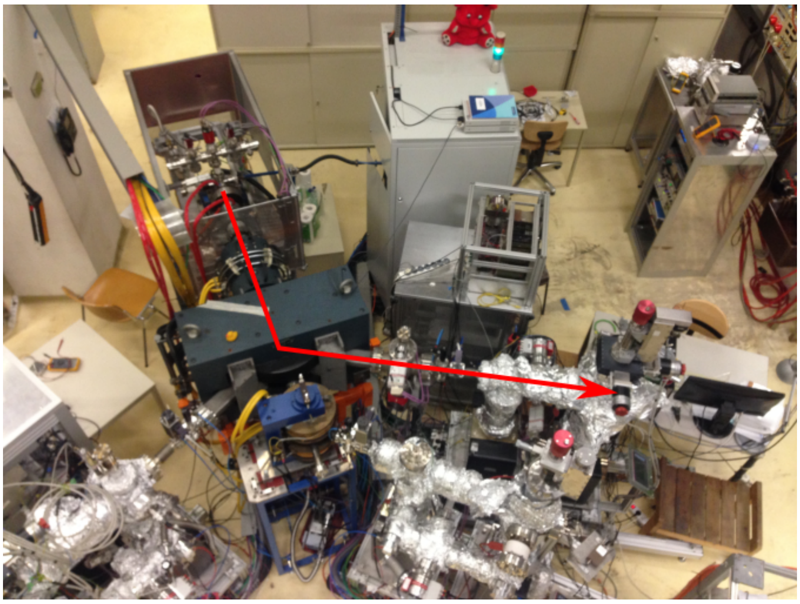

Figure 10: This image shows the AUGSUTIN ion-beam facility, where the experiments presented in this thesis were performed. The ion beam created by an Electron Cyclotron Resonance Ion Source (ECRIS) follows the path indicated by the red arrow. After being extracted from the source and focused by a quadrupole focusing magnet, a sector magnet is used to select a mass over charge state. The beam can then be adjusted using electrostatic deflection plates and an einzel lens to focus the beam into the sample chamber.

disturbance. The mean free path of an ion moving through rest-gas molecules in such a vacuum is in the order of several kilometers, which is why any interactions with residual gas molecules can be neglected. Additionally, QCM experiments are very sensitive to the mass change at the surface of the quartz, which is why they require UHV conditions. Only then the impingment rate of residual gas is low enough to substain clean surfaces over the time of a measurement.

More detailed information on the experimental setup of the ion-beam facility can be found in [33] and [53].

2.2 Quartz Crystal Microbalance (QCM)

The QCM is a method that has been used regularly at the IAP for measuring ion-induced sputtering and implantation effects [29]. It is used to detect small mass changes with sufficient sensitivity to calculate an atomic sputtering yield. In order to investigate the material's properties under ion bombardment, it has to be deposited on the QCM in the form of thin target films. Realizing such targets is possible for a great variety of materials, but this also imposes a restriction on the target sample, which is why the catcher-QCM setup (see Section 2.3) was designed [35].

2.2.1 Measuring Sputter Yields with a QCM

The concept of a QCM as a measurement device for small mass changes is shown in Figure 11. The ion beam hits the target film at an angle of incidence α and sputters surface atoms of the target. Some ions are implanted, while the rest of the beam is reflected from the surface. The QCM acts as a scale that measures the weight change of the target film.

Determining the sputtering yield relies on the piezoelectric property of the quartz [54]. By using a suitable electronic setup, an oscillation at the quartz's resonance frequency can be realized (For details concerning the electronics used at the IAP, which were specifically designed for operating a QCM under UHV conditions, see [29]). The resonance frequency of the QCM is dependent on its thickness and thus mass dependent, assuming a constant quartz density. This can be described by the Sauerbrey equation [55], as the observed mass changes due to ion impact are very small compared to the QCM's mass:

$$\frac{\Delta m\left(\Delta t\right)}{m_Q} = -\frac{\Delta f\left(\Delta t\right)}{f_Q} \tag{2}$$

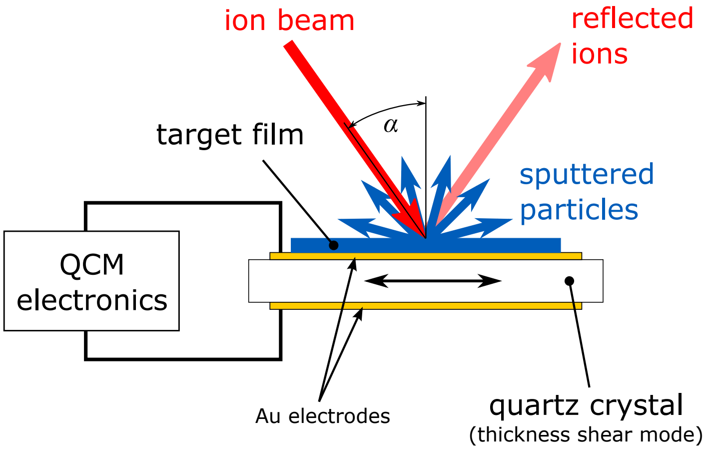

Figure 11: This sketch shows how a QCM is used for sputtering yield measurements. The piezoelectric quartz is part of an oscillating circuit, whose resonance frequency is dependent on the quartz mass. Changes in the target film's mass due to sputtering or implantation then result in frequency changes, which can be measured very precisely.

In this equation, m_Q describes the mass of the oscillating quartz and f_Q its resonance frequency, while Δm and Δf represent the respective changes during a given time period Δt. As frequency variations can easily be measured, this method is used to determine mass changes Δm of the QCM.

However, this quantity alone is not sufficient to calculate the sputter yield, which describes the number of sputtered atoms per incident ion. It is thus necessary to determine how many ions hit the quartz, which is realized by measuring the beam current density j. The number of ions N_{ions} hitting the quartz per unit area during Δt is then given as

$$N_{\text{ions}}\left(\Delta t\right)\left[\text{ion/cm}^2\right] = \frac{\int j dt}{q \cdot e_0} = \frac{j \Delta t}{q \cdot e_0} \tag{3}$$

In this equation, q describes the ions' charge state, e_0 represents the elementary charge and the current density j is assumed to be constant over time. These ions cause a mass change of Δm_A in atomic mass units per unit area:

$$\Delta m_A\left(\Delta t\right)\left[\text{amu/cm}^2\right] = \frac{\Delta m\left(\Delta t\right)}{A_Q m_0} = -\frac{\Delta f\left(\Delta t\right) \cdot m_Q}{f_Q A_Q m_0} = -\frac{\Delta f\left(\Delta t\right) \cdot \rho_Q l_Q}{f_Q m_0} \tag{4}$$

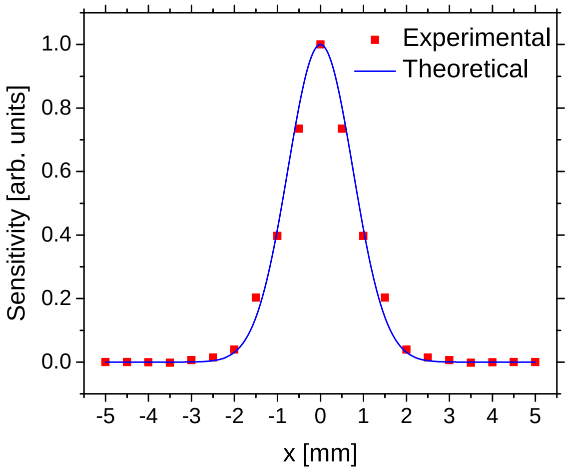

Figure 12: The result of measurements for the radial sensitivity of a QCM. The experimental values for a focused ion beam (red) coincide excellently with the theoretical calculation (blue) based on [56] (see also [53]).

Here the quartz mass is written as $m_Q = \rho_Q l_Q A_Q$ using the quartz's density ρ_Q, its thickness l_Q and its surface area A_Q. Including m_0 leads to Δm_A being described in atomic mass units. The mass removal per ion y is then given as

$$y\,[\text{amu/ion}] = -\frac{\Delta m_A\,(\Delta t)}{N_{\text{ions}}\,(\Delta t)} = q e_0 \cdot \frac{\Delta f\,(\Delta t)}{\Delta t} \cdot \frac{\rho_Q l_Q}{f_Q m_0} \cdot \frac{1}{j} \tag{5}$$

where a mass decrease leads to positive y. Mass changes of a QCM are not only caused by sputtering, but the implantation of ions also has to be taken into account. However, this can be neglected if the projectile ion's mass is significantly smaller than the mass of the sputtered atoms or if steady-state conditions are reached [29]. For composite targets, the sputtering behavior is best described by using the mass removal y. Measuring the frequency change can only give information about the total mass change, but not how the different target elements contribute to it.

For a uniform target, its atoms' standard atomic mass number m_i can then be used to describe the sputter yield as

$$Y\,[\text{atoms/ion}] = \frac{y}{m_i} = \frac{q e_0}{m_i} \cdot \frac{\Delta f\,(\Delta t)}{\Delta t} \cdot \frac{\rho_Q l_Q}{f_Q m_0} \cdot \frac{1}{j} \tag{6}$$

A summary of the quantites used to calculate the sputter yield with a QCM is given in Table 2.

Y	...	sputter yield (number of sputtered atoms per incoming ion)
y	...	mass removal per incoming ion
$\Delta m\,(\Delta t)$	...	mass change of the quartz during Δt
$\Delta m_A\,(\Delta t)$	...	mass change of the quartz in amu per unit area during Δt
$\Delta f\,(\Delta t)$	...	frequency change of the quartz during Δt
$N_{\text{ions}}\,(\Delta t)$	...	number of incoming ions per unit area during Δt
$N_{\text{sp}}\,(\Delta t)$	...	number of sputtered particles during Δt
j	...	current density of the ion beam
q	...	charge state of projectile ions
e_0	...	elementary charge
m_i	...	atomic mass number of the target material
m_0	...	atomic mass unit
m_Q	...	quartz mass
ρ_Q	...	quartz density
l_Q	...	quartz thickness
f_Q	...	quartz resonance frequency
A_Q	...	active area of the quartz

Table 2: An overview of the different quantities used for sputter yield calculation with a QCM.

For practical purposes, equations (5) and (6) can be simplified to

$$y = q \cdot \frac{C}{j} \cdot \frac{\Delta f\left(\Delta t\right)}{\Delta t} \tag{7}$$

and

$$Y = \frac{q}{m_i} \cdot \frac{C}{j} \cdot \frac{\Delta f\left(\Delta t\right)}{\Delta t} \tag{8}$$

where $C = \frac{e_0 \rho_Q l_Q}{f_Q m_0}$ summarizes all remaining constant quantities in the previous equations. The slope of the QCM's output signal $\frac{\Delta f(\Delta t)}{\Delta t}$ is recorded during the measurement process. The ion current density j is determined before and after each measurement with a Faraday Cup (FC) [57] with the additional option of using a beam monitor [58] for taking current variations during the measurement process into account.

With regard to frequency changes due to mass change, the sensitivity of an oscillating quartz decreases radially outwards from its center [55]. It is proportional to the squared shear amplitude of the quartz, which corresponds to a Gaussian function [56]. This property was also investigated experimentally for the QCMs used at the IAP and the result is presented in Figure 12. It shows a normalized comparison of the QCM's frequency change for a focused ion beam hitting the QCM at varying distances to the quartz's center point. For this reason, the curve represents the convolution of the quartz's sensitivity and the beam profile. However, due to the small ion-beam diameter of less than 1 mm, this curve can be used to describe the QCM's sensitivity. This is supported by the theoretical calculation based on the work by Stevens and Tiersten [56] that is included in Figure 12 and fits the experimental data excellently (for details on how to calculate the sensitivity, see [53]).

Measurement of sputtering is thus restricted to the so-called active area where the sensitivity is non-vanishing, while mass changes outside of the active area cannot be registered. However, non-uniform mass removal across the quartz surface can lead to deviations from the Sauerbrey equation (2) [59]. Accordingly, past measurements with a QCM have shown that this method is best suited for determining area sputter yields under uniform ion bombardment [29]. This is realized by scanning the incoming ion beam over the QCM so that the whole active area is exposed to a uniform current density. The beam can be further shaped by using one of several apertures that are included in the sample chamber and can be moved into the beam's path to ensure that the ion beam only hits the target sample.

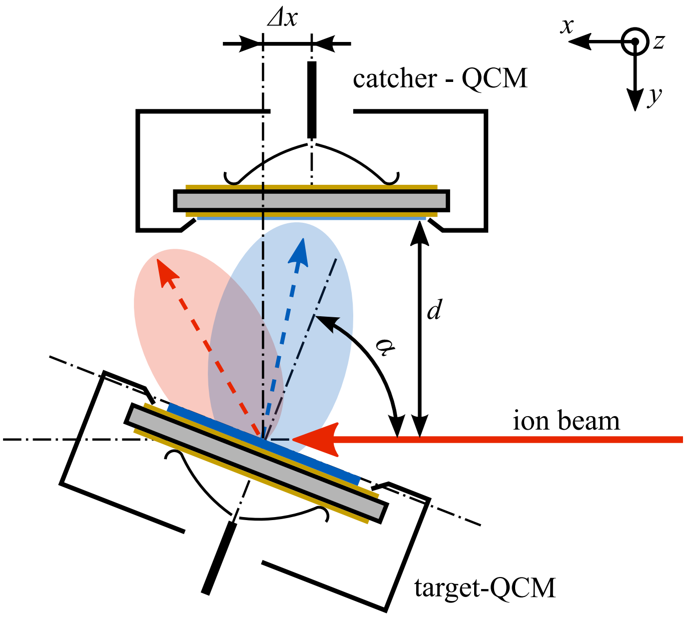

Figure 13: This diagram shows the catcher-QCM setup, where a second QCM is placed beside the target. It is used to measure the amount of sputtered atoms that stick to its surface, and the target sputtering yield Y_{tar} can then be reproduced using a theoretical model. The setup has three variable parameters: The angle of incidence α, the target-catcher distance d and the target shift Δx. (Image taken from [53].)

2.3 Catcher-QCM Setup

2.3.1 Design

The catcher-QCM setup was designed in order to enable sputtering experiments with a larger variety of targets [35]. For direct ion bombardment of a target-QCM a thin film is deposited on the quartz, which poses a restriction on the target material and different effects on the sputtering yield. Especially for complex materials creating thin films with the same composition can be a challenge. Furthermore, properties of the thin film, such as the surface roughness, will be different from that of the original material.

For this reason, a catcher-QCM was placed beside the target holder, as can be seen in the sketch in Figure 13 [35]. The sputtered target atoms are emitted in a cone at energies mostly below 50 eV (see Figure 6 and [37]) and can stick to the catcher surface. The catcher yield Y_C is then measured as the amount of target atoms sticking to the catcher surface per incident ion, which leads to a mass increase of the quartz. However, part of the ion beam is reflected at the target surface and may sputter the catcher-QCM's surface, resulting in a mass decrease. Taking these effects into account, the sputtering yield of the target Y_{tar} can be reproduced using a theoretical model based on SDTrimSP simulations (see Section 3). It should be noted that the target-QCM is included in this setup for proof-of-concept purposes that make it possible to check the feasibility of the catcher setup and the simulations. For future experiments, the target-QCM will be replaced by a rock or a powder target to fully take advantage of the possibilities provided by the new catcher setup.

The catcher setup allows three variable parameters for positioning as indicated in Figure 13. With regard to the coordinate system used in this image, the catcher-QCM itself can only be moved in y-direction, which changes the distance d between target and catcher. Additionally, the orientation of the target and, thus, the angle of incidence α can be changed, as well as the target's position in x-direction, which leads to a target-shift Δx.

Both the target-QCM and the catcher-QCM are mounted in the same mechanical way, which is indicated in Figure 13. There they are fixed in stainless steel holders with springs, where Au electrodes provide the contacts for the electrical signals that drive the quartz oscillations. At each holder heating connectors are included in order to operate the QCM in different temperature ranges that can provide a more stable oscillation [29]. The target sample holder includes a shielded FC that allows beam current density and beam profile measurements before and after an experiment. The target can be rotated around the z-axis so that different angles of incidence up to 75° can be achieved and it is also connected to three stepper motors that allow position changes in x-, y- and z-direction. Due to the fixed direction of the incoming ion beam, however, the latter two variations are only used for measurements of the beam profile.

Measurements with a catcher-QCM require precise control of the ion beam, which must not hit anything outside of the target. For example, atoms sputtered from the steel target holder would also be able to reach the catcher-QCM and thus lead to measurement errors. For this reason a set of circular apertures (Ø2, 3, 4 and 7 mm) mounted on a manipulator was installed in the sample chamber between the scanning plates and the target. By using these apertures the beam size can be controlled very precisely, which is important for evaluating the catcher-QCM's signal. However, the divergence of the scanned ion beam has to be taken into account for determining which aperture to use and for calculating the total beam current hitting the target, which is described in the following section.

More information on this experimental setup can be found in [53].

2.3.2 Evaluation Methods

During sputtering experiments, the frequency changes of the QCMs are recorded and together with the ion-beam current and the quartz's properties, the yields on the target and the catcher can be calculated. In section 2.2.1 the mass removal rate y was derived under the assumption that the Sauerbrey equation (2) is fulfilled (see equation (7)). Following this method, the mass change rate is calculated for both the target- and the catcher-QCM as follows, however, both cases have to be treated separately.

Target-QCM Scanning of the incoming ion beam is performed in order to ensure a homogeneous beam current across the active area of the quartz and, thus, homogeneous sputtering of the surface, which is required for using the Sauerbrey equation in sputter yield calculations. However, ions that do not hit the active area of the quartz do not result in a frequency change. For this reason, the ion-beam current has to be written as the current on the QCM's active area

$$I = \overline{j\left(\alpha\right)} \cdot A_Q \tag{9}$$

The mean of the current densitiy $\overline{j}$ is calculated from FC measurements of the ion-beam profile of the scanned beam

$$\overline{j} = \frac{\overline{I_{\mathrm{FC}}}}{A_{\mathrm{FC}}} \cdot \cos\alpha \tag{10}$$

where I_{FC} is the current measured with the FC and A_{FC} is its area. $\overline{j}$ is dependent on the angle of incidence α because less of the scanned ion beam can hit the active area under non-normal incidence. Additionally, the current at the target is affected by the divergence of the scanned ion beam: Larger Δx mean a greater distance to the scanning plates and thus a wider ion beam. Regarding the active area, this results in a lower current density, which has to be taken into account for mass change rate determination.

The formula for calculating the mass removal rate at the target-QCM y_{tar} can then be simplified as was shown in section 2.2.1, which leads to equation (5):

$$y_{\mathrm{tar}} = q \cdot \frac{C}{\overline{\overline{j\left(\alpha\right)}}} \cdot \frac{\Delta f}{\Delta t} \tag{11}$$

For a single-element target, a sputtering yield per atom can then be derived as shown in equation (8):

$$Y_{\mathrm{tar}} = \frac{y_{\mathrm{tar}}}{m_i} = \frac{q}{m_i} \cdot \frac{C}{\overline{\overline{j\left(\alpha\right)}}} \cdot \frac{\Delta f}{\Delta t} \tag{12}$$

Catcher-QCM The quantity that can be measured with the catcher-QCM is the catcher mass change rate y_{C}, which equals the mass change of the catcher quartz in amu per incoming ion. For single-element targets, the catcher yield Y_{C} is defined as the number of target atoms that stick to the catcher surface, a mass increase of the catcher-QCM thus leads to a positive catcher yield. It should be emphasized that this is contrary to the evaluation of the target-QCM, where a mass removal leads to a positive sputtering yield Y_{tar}.

To calculate the catcher mass change rate, the whole current that hits the target has to be considered. With a QCM target, this also includes the contribution of ions that hit outside of the active area, as their sputtering behavior is the same as for other ions. As long as it can be guaranteed that the whole ion beam hits the target, the current is not dependent on the angle of incidence. However, scanning the ion beam larger than the target should be avoided at all costs, because sputtering of the surrounding target holder would then also occur and influence the catcher yield. For this reason, the scanned ion beam can be controlled with a set of apertures with known diameters as described in the previous section in order to ensure sputtering only of the film deposited on the target-QCM.

As a result, the number of ions hitting the QCM per unit area during Δt $N_{\mathrm{ions}}\left(\Delta t\right)$ [ion/cm^2] in equation (3) has to be replaced by the total number of ions hitting the target-QCM in the same time span

$$N_{\mathrm{ions}}^{\mathrm{total}}\left(\Delta t\right)\left[\mathrm{ion}\right] = \frac{I\Delta t}{q \cdot e_0} \tag{13}$$

The mass change per unit area $\Delta m_A\left(\Delta t\right)$ [amu/cm^2] during Δt in equation (4) has to be similarly adapted, which instead becomes the total mass change during Δt

$$\Delta m\left(\Delta t\right)\left[\mathrm{amu}\right] = \frac{\Delta m\left(\Delta t\right)}{m_0} = -\frac{\Delta f\left(\Delta t\right) \cdot \rho_Q l_Q A_Q}{f_Q m_0} \tag{14}$$

The catcher mass change rate y_C is then defined as

$$y_C\,[\text{amu/ion}] = \frac{\Delta m\,(\Delta t)}{N_{\text{ions}}^{\text{total}}\,(\Delta t)} = q \cdot \frac{C^*}{I} \cdot \frac{\Delta f\,(\Delta t)}{\Delta t} \tag{15}$$

with $C^* = C \cdot A_Q = \frac{e_0 \rho_Q l_Q A_Q}{f_Q m_0}$ including the QCM's active area. The total ion beam current I can be derived from the measured FC current $\overline{I_{\text{FC}}}$ by taking into account the area of the aperture and the divergence of the scanned ion beam:

$$I = \frac{\overline{I_{\text{FC}}}}{A_{\text{FC}}} \cdot \left(r_{\text{ap}} + s_x \cdot \tan\beta\right)^2 \cdot \pi \tag{16}$$

Here $A_{\text{ap}} = r_{\text{ap}}^2 \cdot \pi$ describes the aperture area used, s_x is the distance between the aperture and FC in x-direction and β represents the divergence angle of the ion-beam scanning. The expression in brackets in equation (16) thus describes the radius of the area where the scanned ion beam hits the target. This has to be included as the ion beam broadens after passing the aperture and irradiates an area on the QCM larger than A_{ap}.

2.3.3 The parameter g

Using the catcher-QCM setup with a target-QCM is a feasible way of investigating sputtering behavior in regard to angular dependencies of sputtered material or reflected ions. However, when using targets that do not allow direct sputtering measurements in the same way as with a QCM, the interpretation of the catcher signal is very important. The goal for solar-wind-effect measurements is, for example, directly bombarding a piece of stone and measuring only the catcher mass change rate y_C. In order to calculate the target mass removal rate y_{tar}, exact knowledge of the expected angular distributions, the sputtering at the catcher-QCM by reflected ions and the sticking of sputtered material is required.

In order to describe the relation of target and catcher, the parameter $g = y_C / y_{\text{tar}}$ is defined, which describes the ratio between the mass change of the catcher and the target. g can be determined experimentally with a target- and a catcher-QCM, but can also be calculated theoretically. The latter is necessary for the reconstruction of the target mass change $y_{\text{tar, rec}} = y_{\text{C, exp}} / g_{\text{sim}}$ with the measured catcher mass change $y_{\text{C, exp}}$ and a simulated parameter g_{sim}. The simulation is based on the geometric analysis of SDTrimSP calculations, which is the topic of Section 3.

First proof-of-principle measurements with two QCMs (see Section 4.1 and [35]) were performed with the goal of comparing experimental and calculated g values to

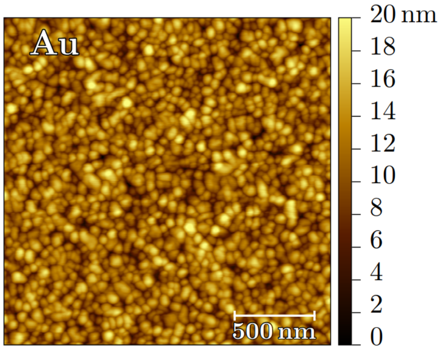

Figure 14: The Atomic Force Microscopy (AFM) image of the Au-coated QCM shows a regular island pattern. The RMS value of the surface roughness has been found to be rather low, at 2.9 nm, and thus the sample can be considered as flat. (Image taken from [53].)

show the feasibility of the setup. This was continued with Fe targets of different roughness - an aspect that is not included in conventional SDTrimSP simulations, instead a simulation approach using the expansion SDTrimSP-2D was used (see Section 4.2). Finally, Wollastonite-coated QCMs were investigated to look at catcher measurements for composite targets and to compare the catcher mass change rate to values observed by directly bombarding a stone (Section 4.3).

2.4 Sample Preparation and Analysis

2.4.1 Au QCM-Films

A substantial amount of literature data exists for the projectile target combination Ar and Au, and Au-targets are comparably easy to handle considering contaminations. For this reason, Au was chosen for performing first proof-of-concept measurements with the catcher setup. Mutliple QCMs with a thin Au film created with sputter deposition were provided by Prof. Eisenmenger-Sittner from the Institute of Solid State Physics at TU Wien.

AFM In order to analyze the structure of the surface, one Au QCM was investigated with an Atomic Force Microscope (AFM). Using a nm-scale tip mounted on a cantilever, surfaces can be investigated with an AFM by measuring the cantilever's distortion due to interatomic forces between sample and tip [60]. This makes it possible to record images at nm resolution, as seen in Figure 14 for the Au-coated QCM. Small island structures can be seen there that result in a root mean square (RMS) value of the surface roughness of 2.9 nm [53]. Compared to the Fe samples that were also used in this thesis (see the following section 2.4.2), this value is rather low and for this reason the Au targets were considered as flat in the simulations.

2.4.2 Fe QCM-Films

For the investigation of Fe targets with different surface roughness, multiple sputter deposited quartzes were supplied by the Max-Planck-Institute of Plasma Physics (IPP) Garching. It was decided to use such samples with different surface roughnesses for experiments with the catcher setup in order to investigate the influence of this surface structure on the catcher signal. The target's surface roughness represents a very important aspect of future experiments with stone or powder samples. For this reason, the influence of this quantity is first investigated with the thin film QCMs, which are much easier to interpret due to the possibility of direct sputtering yield measurements. The sputtering behavior of these QCMs for different angles of incidence and under long-term irradiation had also been investigated at IAP beforehand [61].

AFM As a part of the above-mentioned experiments, AFM images of the Fe-coated QCMs were taken before and after irradiation. Initially, grain-like features are visible that change during the ion bombardment (under an incident angle of 60 degrees) due to the sputtering to a ripple structure that is strongly aligned with the direction of incoming ions.

During the irradiation a surface smoothening also occurs, which can be quantified by the distribution of local angles, which denote the angle between the local surface normal and the z-axis. This distribution can be calculated from the AFM data and a comparison between this distribution of angles before and after irradiation is shown in Figure 16. The distribution of the initial rough surface (red) has a peak at around 20 degrees and is very broad compared to the distribution after the irradiation (blue). As a perfectly flat surface would be represented by a delta distribution centered at 0 degrees, the surface can be interpreted as much smoother after the irradiation. Furthermore, a decrease of the root mean square (RMS) roughness from about 5.2 to 3.5 nm was found [61].

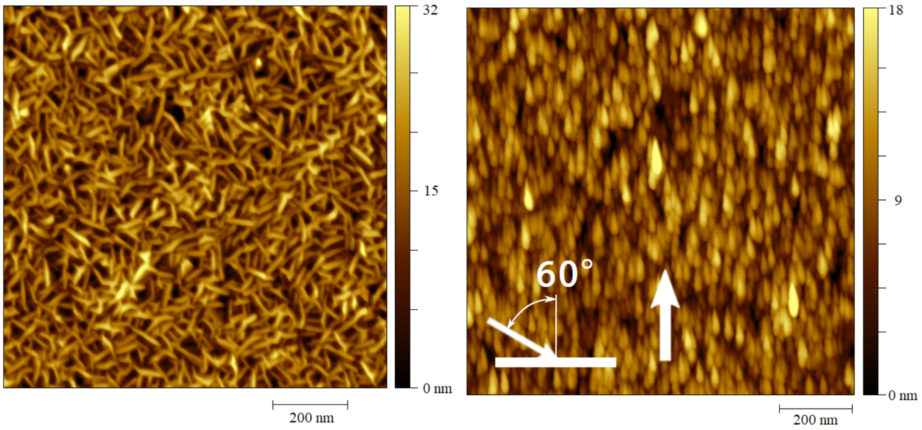

Figure 15: AFM images of the target before (left) and after an irradiation with $6.7 \cdot 10^{21}\,\mathrm{Ar/m^2}$ show the change of the surface structure [61]. Grain features that can be observed on an unirradiated sample transform into ripple-like structures, which are clearly aligned with the direction of irradiation (indicated by the white arrow). (Images adapted from [61].)

XPS As the QCM technique only allows the measurement of the total mass change of the quartz and the presence of an oxide layer on the Fe film was assumed, one Fe-QCM was analyzed using X-Ray Photoelectron Spectroscopy (XPS). XPS measures the energy spectrum of photoelectrons emitted from a sample due to X-Ray exposure. It represents a very good method for quantitative elementary analysis, which also gives insight into chemical bonds of the elements [62]. The Fe-coated quartz was examined with a sputter-XPS setup, which allows repeated XPS measurements after sputtering away some layers of target material with a sputter gun. This results in a depth-profile for the sample composition, which is shown in Figure 17 for the Fe sample. It shows a high concentration of O at the surface, but even in the bulk the Fe concentration only reaches up to 85%, which has to be taken into account for correct interpretation of the measurement results.

Conclusion Fe-coated QCMs before and after long-term irradiation are well-suited targets for investigating different surface roughnesses due to the smoothening that occurs during irradiation. As both samples that were investigated as part of this thesis had been stored for several months before the experiments, they will show a significant O concentration with C and N impurities both at the surface and in

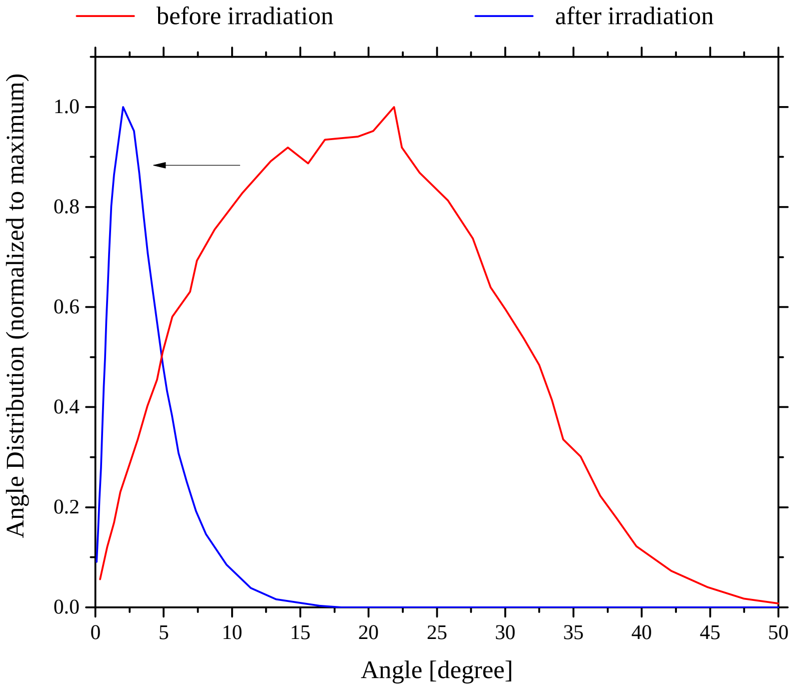

Figure 16: The distribution of the angles between the nominal z-axis and the local surface normals, which were calculated from the AFM images in Figure 15, shows a shift towards lower angles and a decrease of its width after ion-beam irradiation. This can be interpreted as a smoothening of the surface, since an ideally flat sample would correspond to a delta distribution at 0 degrees.

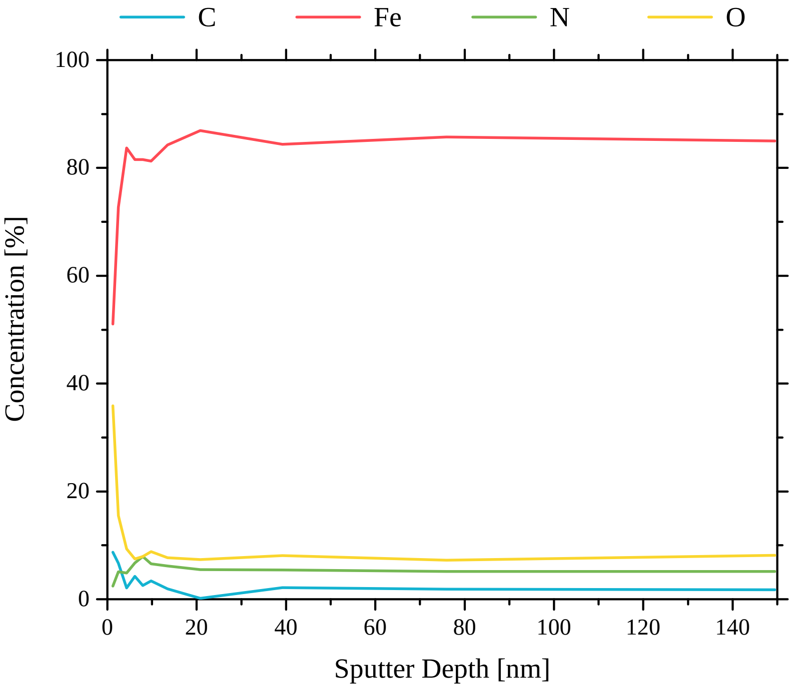

Figure 17: This plot gives an overview of the XPS analysis of a Fe-coated QCM for different depths, which was performed at the Analytical Instrumentation Center of TU Wien. A significant oxide layer on top of the sample can be seen, where the Fe concentration is only about 50% and the O concentration is about 35%. However, even the bulk Fe concentration only reaches about 85%, which has to be taken into account for precise SDTrimSP simulation.

the bulk. For correct simulation of these experiments, both the composition and the surface roughness have to be taken into account.

2.4.3 Wollastonite ($CaSiO_3$)

The mineral Wollastonite ($CaSiO_3$) has a similar chemical composition to the pyroxene group (for example, Enstatite ($MgSiO_3$) and Ferrosilite ($FeSiO_3$)), but it is regarded seperately due to differences in crystal structure ([36], [63]). On Earth it occurs regularly in limestone and can be found across most continents [63]. Its applications are found in different material manufacturing processes, but most importantly Wollastonite has been used as a bioactive ceramic [64]. For the purpose of planetary research it is relevant as rock samples from the Moon provided by the Apollo missions showed an abundance of pyroxene minerals [36]. Experiments with a Wollastonite sample thus provide an interesting opportunity to investigate solar-wind effects on the lunar surface.

While measuring the sputtering of the stone due to ion bombardment represents the most relevant experiment for investigating solar-wind effects, there are many uncertainties connected to these measurements. Compared to a thin film, angular distributions of the particles hitting the catcher may be different and sticking coefficients, especially from O, may be less than 1 [65]. Furthermore, due to Wollastonite's insulating nature, potential sputtering is expected to occur [31]. The different chemical potentials and the crystal structure of bound $CaSiO_3$ that are not included in SDTrimSP correctly can also lead to inaccuracies in the simulation.

For this reason, it was decided to first investigate a thin Wollastonite film deposited on a QCM. Due to direct information on the sputtering it becomes easier to explain possible deviations from the simulated behavior. Furthermore, using a catcher-QCM with target material should maximize the sticking coefficient of the sputtered material. Thus, establishing the sample preparation and analysis techniques presented in this section is also helpful for future experiments with other composite materials.

Sample Preparation The original mineral sample was provided by Prof. Peter Wurz (Physics Institute, University of Bern) and Prof. Klaus Mezger (Institute of Geological Sciences, University of Bern) (see Figure 18). In order to use it for deposition and analysis, it was cut into multiple pieces using a diamond saw and a

Figure 18: This image shows the original Wollastonite piece that was provided by the University of Bern. All samples for deposition and analysis for this thesis are originally from this rock.

Stanley knife. The pieces were then polished using a wet-grinding machine in the IAP workshop. In order to remove the water that the stone absorbed during the grinding process, a small vacuum chamber was prepared for baking the stone pieces, where each one of them was heated at 320 °C for three days under rough vacuum conditions.

PLD As mentioned before, besides directly bombarding the stone with ions and measuring the sputtered material with the catcher-QCM, irradiating a Wollastonite layer deposited on a QCM gives additional information about the sputtering behavior of Wollastonite. Pulsed Laser Deposition (PLD) is generally accepted as the best technique to realize thin stoichiometric films from a composite sample [66]. Laser pulses are thereby directed onto a target, here one of the prepared Wollastonite stone pieces, where they create a plasma plume from the target material. This plume hits the substrate where a layer of the target material is deposited. Using this technique, Wollastonite films were deposited on two QCMs as well as several silicon wafer pieces by Michael Doppler and Prof. Jürgen Fleig (Institute of Chemical Technologies and Analystics, TU Wien). PLD was performed with a 248 nm

KrF excimer laser at a pulse frequency of 5 Hz and a pulse energy of 5 mJ while the sample was kept at about 250 °C. The deposition times of the QCMs were 30 and 60 minutes with the latter being used as the target so that more material would be available for sputtering.

XRD Directly after the laser deposition, Michael Doppler investigated the film growth using X-Ray diffractometry (XRD). XRD is a very important tool in crystallography, which uses the photons scattering at atom's electron clouds to determine its crystallic structure. X-Ray photons are diffracted at the lattice and interfere constructively following Bragg's law $n \cdot \lambda = 2d \cdot \sin\theta$ [67]. The visible peaks of the XRD-measurements show only the Au layer of the QCM, while no diffraction from any Wollastonite was observed. However, this method only registers X-Ray photons diffracted from a regular crystal structure, while no signal from an amorphous solid can be measured. As a result, the XRD analysis cannot tell whether an amorphous layer of Wollastonite has formed or if there is no dense film at all. This information would be important for judging the feasibility of using these QCMs for experiments where a thorough layer of Wollastonite is necessary. Otherwise, sputtering of the QCM's Au electrode would also occur and lead to false results as only the absolute mass change rate can be measured with a QCM.

AFM The Wollastonite-coated QCMs and the deposited Si samples were examined in an Atomic Force Microscope (AFM) that is available at IAP. Figure 19 shows two images by Daniel Mayer (IAP) of a deposited QCM where several round patterns with a size of up to 1 μm can be observed, while the surface otherwise seems to have a roughness in the nm scale, but looks dense on the AFM images. These results give a good insight into the structure of the QCM surface, but not its composition. While one possibility is that only small Wollastonite clusters were deposited onto the Au layer the PLD may also have caused a non-uniform film growth. Fernández-Pradas et al. observed such a rough structure on PLD pseudowollastonite coatings that had to be exposed to an additional laser treatment in order to create a flat surface [68]. However, promoting more uniform film formation by heating and annealing is limited by the QCM's phase transition from an α- to a β- quartz at 573 °C [69].

XPS and TOF-SIMS In order to get a definite answer about the surface composition of the samples, they were investigated with X-Ray Photoelectron Spectroscopy

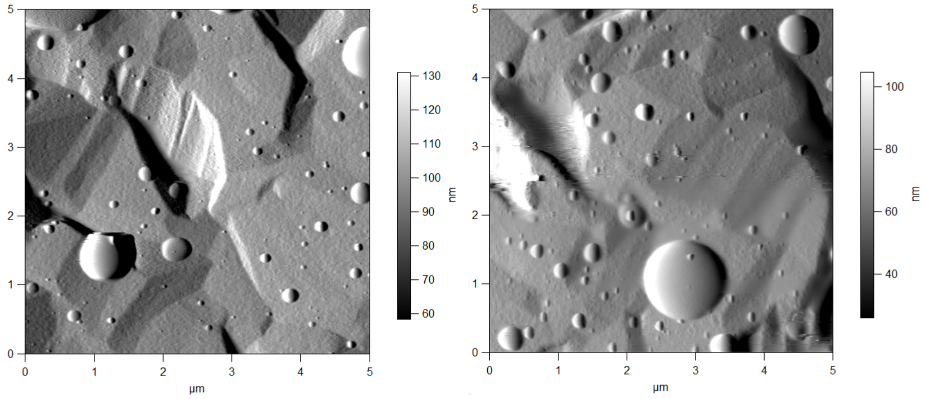

Figure 19: These two pictures show AFM images taken from the QCM surfaces after PLD, where easily recognizable circular patterns can be seen at multiple points. Their size varies widely, but is generally found to be in the nm range. The AFM images give no information about whether they represent a rough Wollastonite surface or Wollastonite clusters on the QCM's Au layer.

(XPS) and Time of Flight Secondary Ion Mass Spectroscopy (TOF-SIMS). TOF-SIMS measures which secondary ions are emitted from the sample as a result of sputtering by ion bombardment. Compared to the quantitative XPS, it is more suited for qualitative analysis with a detection limit in the parts per million (ppm) to parts per billion (ppb) range with a good lateral solution and the possibility of performing depth-dependent measurements. Due to large variations in the secondary ion yield, which is heavenly dependent on the sample, quantification of SIMS signals, however, is very complicated.

The XPS analysis was performed by Markus Sauer (Analytical Instrumentation Center, TU Wien) with the result shown in Figure 20. The upper two spectra represent the signals for two of the Si wafer pieces that were also deposited with a Wollastonite layer for analysis purposes. The lower two spectra were taken with Wollastonite powder pressed onto C tape and In tape respectively. Si wafer pieces were used here in order to avoid scratching the sensitive QCM surface, while the usage of powder was necessary to avoid charging up effects during the XPS analysis. It is evident that all four samples show very similar spectra with minor differences in their composition such as a higher Ca abundance and the presence of N in the powder sample, which may originate from the storage in air or from the grinding process (see Table 3 for exact results of the XPS analysis). For the deposited films, an

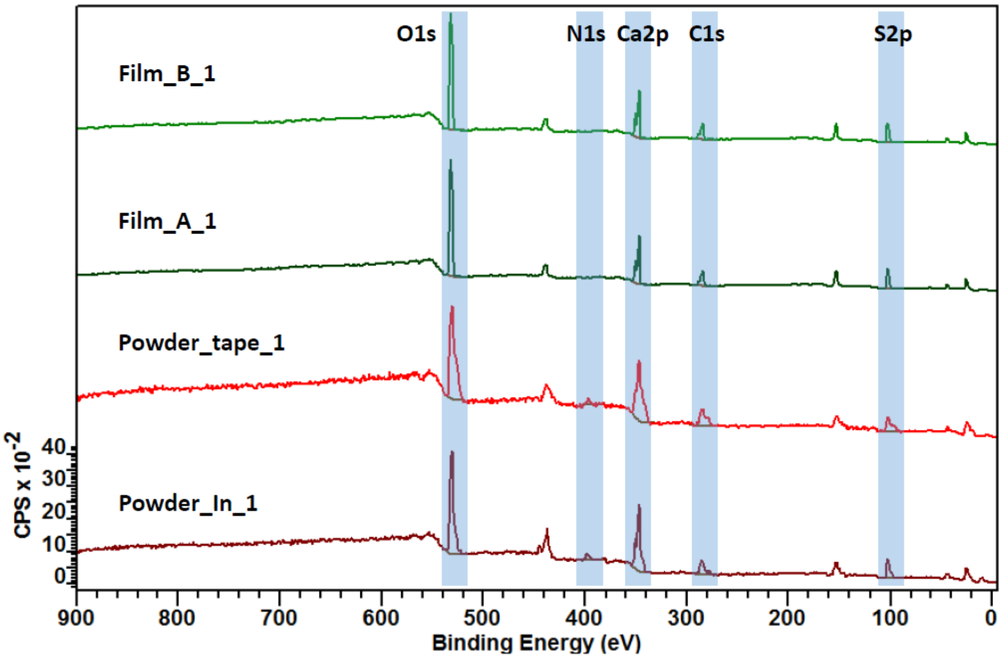

Figure 20: This graph shows the XPS spectra for two Si wafer pieces (Film_B_1 and Film_A_1), Wollastonite powder on conducting C tape (Powder_tape_1) and powder on In foil (Powder_In_1). The signals show a similar composition of the respective surfaces with a higher Ca abundance being observed in the powder (for details see Table 3).

	Element [at. %]					**Relations**		
Sample	**C**	**Ca**	**N**	**O**	**Si**	**Ca/Si**	**Ca/O**	**Si/O**
Powder (In tape)	19.7	15.5	5.5	45.4	13.9	1.2	0.35	0.31
Powder (C tape)	23.8	16.1	2.7	44.4	13.1	1.2	0.36	0.30
Film A	17.4	12.7	0.0	53.7	16.2	0.78	0.24	0.30
Film B	19.5	12.2	0.0	52.5	15.7	0.78	0.23	0.30
$CaSiO_3$	-	20.0	-	60.0	20.0	1.0	0.33	0.33

Table 3: An overview of the quantitive results of the XPS measurements for the powder on In and C tape as well as the films on two Si wafer pieces. The results are the mean values for two spots and have a relative error of about 10%. For reference purposes, the respective values for the nominal composition $CaSiO_3$ are included, showing that the composition of the samples is very similar to the expected Wollastonite composition.

average composition of 15.3 % Ca, 19.6 % Si and 65.1 % O derives from disregarding the C content which is assumed to be a surface contamination originating from air exposure. A more detailed investigation of the Si contribution to the spectrum shows only a singular peak, while Si wafers normally show a dual peak of the Si bulk and an SiO_2 layer on top [70]. With a spot size of 500 μm and no such features to be seen it should thus be expected that the whole contribution to the Si peak comes from the Wollastonite ($CaSiO_3$).

TOF-SIMS was then used to examine the deposited layer on the two QCMs. For both samples, the secondary ions were analyzed for different depths and the results for one QCM are shown in Figure 21. This was realized by continuously sputtering a small area with a second ion beam, besides the original ion beam that is used for secondary ion creation. The measurement was taken at the edge of the QCM where the oscillating behavior of the quartz is hardly influenced. Due to uncertainties in the ion current of the second beam, the secondary ion intensity is plotted over sputtering time in Figure 21. Limitations are also present for the interpretation of the intensity as the ionization probability varies very widely for different elements and the chemical properties of the investigated sample. However, the TOF-SIMS results for both samples show the presence of the Wollastonite elements Ca, Si and O or their combinations in the beginning, where the underlying Au cannot be seen

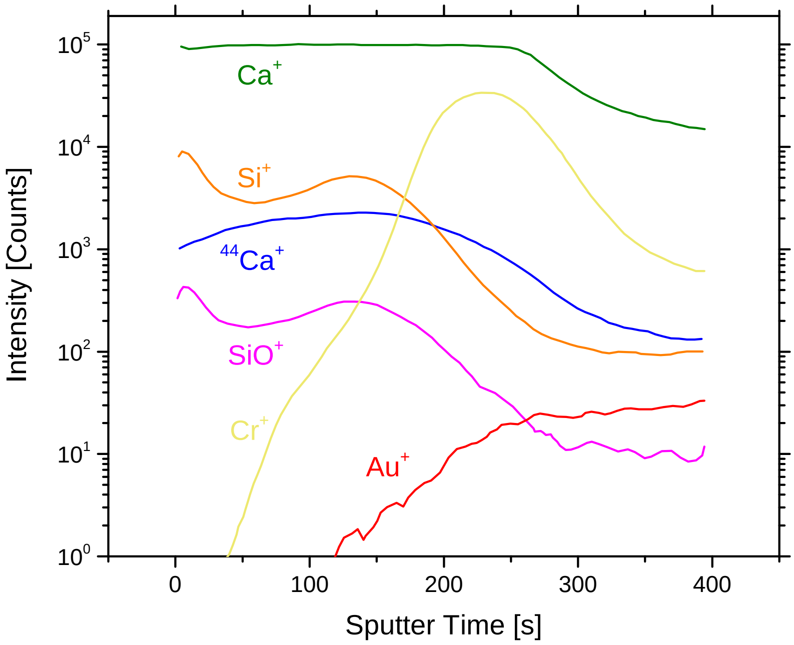

Figure 21: This graph shows the TOF-SIMS results for one of the two QCMs that were deposited with Wollastonite. Measured secondary ion intensity is plotted over sputtering time for different ions and thus represents an indicator for the changes in concentration with depth. Both samples show a well-pronounced layer of the Wollastonite components Ca, Si and SiO and afterwards the Cr and Au layers on top of the quartz. The constant Ca signal for low sputtering times is due to the measurement signal reaching the upper intensity limits of the secondary ion detection.

at all. Only after sputtering away the top layers of the material the Au signal and a Cr layer covering the electrod can be seen, which is connected to a decrease in the intensity for the ions of the elements of Wollastonite.

Conclusion Despite originally being indicated otherwise, XPS and TOF-SIMS conclusively lead to the result that a dense layer of Wollastonite material has formed on top of the QCMs during PLD. They are thus suited for usage during sputtering experiments to investigate the effects of ions hitting Wollastonite and comparing the results to sputtering of the original rock sample. It should however be noted that differences in behavior are to be expected due to the amorphous structure of the thin film, the differences in composition (Ca abundance) and the surface features observed with the AFM.

3 Theoretical Description of Catcher Measurements

The goal of the catcher setup is the investigation of sputtering behavior without direct measurements at the target. This is realized by calculating the mass change of the catcher-QCM and using this information to determine the mass removal at the target.

In order to theoretically describe the measured catcher signal, two contributions have to be taken into account:

- sticking of atoms that were sputtered from the target to the catcher surface
- sputtering of the catcher surface by projectiles that were reflected by the target and hit the catcher

Further surface erosion at the catcher by sputtered atoms from the target is ignored because of their low kinetic energy (see section 1.2.3). It should be noted that implantation of projectile ions was ignored during the simulations described in this section. The mass change of the catcher per projectile ion represents the increase due to the sticking of sputtered atoms ($y_{\mathrm{C,sp}}$) minus the contribution of sputtered atoms caused by reflected ions ($y_{\mathrm{C,r}}$). The measured mass change rate at the catcher y_{C} can therefore be described as the difference between these quantities:

$$y_{\mathrm{C}} = y_{\mathrm{C,sp}} - y_{\mathrm{C,r}} \tag{17}$$

3.1 Calculating y_{C}

3.1.1 Contribution of Sputtered Atoms

The mass increase at the catcher caused by the sticking of sputtered atoms $y_{\mathrm{C,sp}}$ is dependent on the sputtering at the target, the angular distribution of the sputtered atoms and the position of the catcher, which can be described by the angle of incidence α, a displacement Δx of the target in the ion beam's direction and the distance d between the target and the catcher (see Figure 13). Furthermore, sticking coefficients S^i for each target element i have to be taken into account to describe the only partial surface adsorption of atoms reaching the catcher. These dependencies can be combined in factors $y^i_{\mathrm{C,sp}}$ describing the catcher mass change

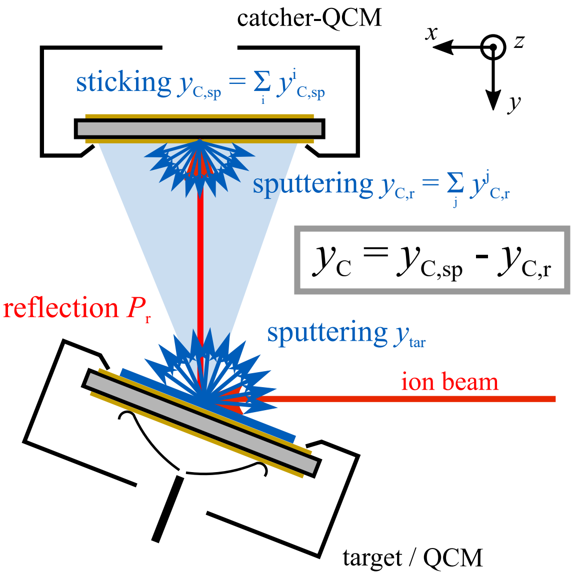

Figure 22: An overview of the different effects that have to be taken into account for the calculation of the catcher mass change rate.
Ions hitting the target cause sputtering of the surface material causing a mass removal rate y_{tar} and are reflected with a probability P_{r}. A fraction of the sputtered atoms reaches the catcher and sticks to its surface, the corresponding mass change rate can be described by $y_{\text{C,sp}} = \sum_i y^i_{\text{C,sp}}$. Additionally, reflected ions can sputter atoms from the catcher, causing a mass change rate of $y_{\text{C,r}} = \sum_j y^j_{\text{C,r}}$. Erosion of the catcher surface by sputtered target atoms is ignored, owing to their low kinetic energies. Combining these effects, the catcher mass change rate is then given as $y_{\text{C}} = y_{\text{C,sp}} - y_{\text{C,r}}$.

rate caused by the sticking atoms of the element i. $y_{\mathrm{C,sp}}$ can be derived by summing the contributions of all target elements i:

$$y_{\mathrm{C,sp}} = \sum_i y^i_{\mathrm{C,sp}} \tag{18}$$

In order to specifiy $y^i_{\mathrm{C,sp}}$, the number of sputtered atoms that can be measured with the catcher has to be calculated. The target is therefore assumed to be on the xy-plane with its center being the origin of the coordinate system. Ions hitting the target at the point (x, y) cause target atoms of element i to be sputtered in the solid angle Ω with a angular distribution $f^i_{\mathrm{sp}}\left(\Omega, x, y\right)$ with

$$\int_{2\pi} f^i_{\mathrm{sp}}\left(\Omega, x, y\right) d\Omega = 1 \tag{19}$$

Sputtered atoms do not originate at the same point, but across the area of the beam cross section represented by the current density $j\left(x, y\right)$ with

$$\int_{A_{\mathrm{tar}}} j\left(x, y\right) dA = I \tag{20}$$

Here j is integrated over the target surface A_{tar} and I represents the total current of the ion beam.

Sputtered atoms originating from points with high current density will add a greater contribution to the total resulting angular distribution $\widetilde{f^i_{\mathrm{sp}}}$ of sputtered atoms of element i. For this reason, the product of j and f^i_{sp} has to be integrated over the beam cross section in order to calculate $\widetilde{f^i_{\mathrm{sp}}}$:

$$\widetilde{f^i_{\mathrm{sp}}}(\Omega) = \frac{1}{I} \int_{A_{\mathrm{tar}}} \Big[j\left(x, y\right) \cdot f^i_{\mathrm{sp}}\left(\Omega, x, y\right) \Big] dA \tag{21}$$

The division by I is necessary for the normalization of the integral.

For the description of the measured signal at the catcher, this distribution has to be weighted with the QCM's sensitivity $s\left(r_{\mathrm{C}}\right)$. The value of s is dependent on where a sticking atom hits the catcher surface, which is only dependent on the distance r_{C} from its center point (see Figure 12). The position and direction of the catcher surface are dependent on the parameters α, d and Δx. For the calculation of $y^i_{\mathrm{C,sp}}$, however, the only relevant dependence of s is the solid angle Ω. The limited size of the quartz's active area is considered in the sensitivity $s(\Omega)$, and for this reason the integration can be performed over all angles. How $r_{\mathrm{C}}(\Omega)$ and thus $s(\Omega)$ can be calculated exactly is described in detail later in section 3.2.1. In order to obtain the final result for the mass change rate $y^i_{\mathrm{C,sp}}$, the integral over the spatial distribution has to be multiplied with the target mass removal rate y_{tar} as the sputtering of the target determines how many sputtered atoms can reach the catcher. Assuming a constant sticking coefficient S^i leads to the following expression:

$$y^i_{\mathrm{C,sp}} = y_{\mathrm{tar}} \cdot S^i \int_{2\pi} \left[\widetilde{f^i_{\mathrm{sp}}}(\Omega) \cdot s(\Omega) \right] d\Omega =$$

$$= y_{\mathrm{tar}} \cdot \frac{S^i}{I} \int_{A_{\mathrm{tar}}} \int_{2\pi} \left[j\left(x,y\right) \cdot f^i_{\mathrm{sp}}\left(\Omega, x, y\right) \cdot s\left(\Omega\right) \right] d\Omega dA \tag{22}$$

3.1.2 Contribution of Reflected Ions

Looking at the reflected ions, the results are similar to the sputtered atoms' contribution. The catcher mass removal rate $y_{\mathrm{C,r}}$, which describes sputtering of catcher material by reflected ions, is dependent on the reflection probability P_{r}. The mass removal rates $y^j_{\mathrm{C,\ r}}$ of the catcher elements j are used to describe the relation

$$y_{\mathrm{C,r}} = \sum_j y^j_{\mathrm{C,r}} \tag{23}$$

Equivalent to f^i_{sp}, f_{r} is used to describe the distribution of the reflected ions originating from (x,y). In contrast to before, the number of reflected ions that hit the catcher alone is not of importance, but the sputtered atoms of element j caused by these ions are. One ion hitting the catcher causes a mass removal of $y^j\left(\alpha_r, E\right)$, which is dependent on the ions' angle of incidence α_r on the catcher surface and the ions' energy E. For this reason, the energy distribution has to be included in $f_{\mathrm{r}}\left(\Omega, x, y, E\right)$ with

$$\int_0^\infty \int_{2\pi} f_{\mathrm{r}}\left(\Omega, x, y, E\right) d\Omega dE = 1 \tag{24}$$

With regard to the beam-current profile, the same arguments that were used to derive equation (22) apply here. Again, a resulting spatial distribution of the reflected ions $\widetilde{f_{\mathrm{r}}}(\Omega, E)$ can be defined as follows:

$$\widetilde{f_{\mathrm{r}}}(\Omega, E) = \frac{1}{I} \int_{A_{\mathrm{tar}}} \left[j\left(x,y\right) \cdot f_{\mathrm{r}}\left(\Omega, x, y, E\right) \right] dA \tag{25}$$

Similar to r_{C}, the angle of incidence on the catcher surface α_r is only dependent on the solid angle Ω. Its detailed calculation can also be found in section 3.2.1. Finally, the calculation of $y^j_{\mathrm{C,r}}$ requires the multiplication of the integral by the reflection probability P_{r}. Taking these aspects into account, $y^j_{\mathrm{C,r}}$ can be written as

$$y^j_{\mathrm{C,r}} = P_{\mathrm{r}} \cdot \int_0^\infty \int_{2\pi} \left[\widetilde{f}_{\mathrm{r}}(\Omega, E) \cdot y^j(\Omega, E) \cdot s(\Omega) \right] d\Omega dE =$$

$$= P_{\mathrm{r}} \cdot \frac{1}{I} \int_{A_{\mathrm{tar}}} \int_0^\infty \int_{2\pi} \left[j\,(x, y) \cdot f_{\mathrm{r}}\,(\Omega, E, x, y) \cdot y^j\,(\Omega, E) \cdot s\,(\Omega) \right] d\Omega dE dA \tag{26}$$

3.1.3 Conclusion

By calculating the respective mass change rates $y^i_{\mathrm{C,sp}}$ and $y^j_{\mathrm{C,r}}$, the combined factor g with $y_{\mathrm{tar}} = y_{\mathrm{C}}/g$ can be theoretically described:

$$y_{\mathrm{C}} = y_{\mathrm{C,sp}} - y_{\mathrm{C,r}} = \sum_i y^i_{\mathrm{C,sp}} - \sum_j y^j_{\mathrm{C,r}} = g \cdot y_{\mathrm{tar}}$$

$$\Rightarrow g = \frac{\sum_i y^i_{\mathrm{C,sp}} - \sum_j y^j_{\mathrm{C,r}}}{y_{\mathrm{tar}}} \tag{27}$$

This combined factor g is well-suited for a comparison between experimental and theoretical results. On the one hand, both y_{C} and y_{tar} can be measured simultaneously by using a target-QCM. On the other hand, both quantities and thus the factor g can be calculated in a simulation, which is described in the following section.

In case of targets consisting of only one chemical element, the theoretical description of the parameter g can be simplified, as is described in [35]. As both the target and the catcher are made up of the same element, the sums over i and j can be omitted. It is also more convenient to characterize the sputtering behavior using the sputtering yield $Y = y/m_i$ with m_i being the mass of the investigated element in amu. The mass removal rates y in equation (26) and y_{tar} in equation (27) can therefore be replaced by the respective sputtering yields Y and Y_{tar}. Instead of $y_{\mathrm{C,sp}}$ and $y_{\mathrm{C,r}}$ the yields $Y_{\mathrm{C,sp}} = g_{\mathrm{sp}} \cdot Y_{\mathrm{tar}}$ and $Y_{\mathrm{C,r}}$ can be used. By defining the parameter g_{sp} that only describes the contribution to g by the sputtered atoms sticking on the catcher, the target yield Y_{tar} can be cancelled. This leads to the following expression for g:

$$g = \frac{Y_{\mathrm{C,sp}} - Y_{\mathrm{C,r}}}{Y_{\mathrm{tar}}} = g_{\mathrm{sp}} - \frac{Y_{\mathrm{C,r}}}{Y_{\mathrm{tar}}} \tag{28}$$

3.2 SDTrimSP Simulations

Simulations of ion surface interaction under varying angles of incidence were performed with the program SDTrimSP, which was developed at the Max Planck Institue for Plasma Physics [38]. SDTrimSP is a Monte Carlo simulation that calculates the trajectories of incoming ions hitting amorphous solids with a binary collision model. By redesigning the software structure, it represents an advanced version of TRIDYN, a simulation program that uses similar computational models [71]. The primary purpose of simulating ion surface interaction is the analysis of sputtering as well as changes in the surface composition and depth profiles under ion bombardment ([38], [72]). In comparison to similar programs, SDTrimSP has been shown to give better results especially considering sputtering measurements under skew incidence [73], which are of specific interest for this thesis.

Knowledge of the number of sputtered particles is sufficient to reproduce the mass removal rate of the ion beam's target. However, further information is needed to calculate the expected number of particles hitting the catcher QCM, as it is heavily dependent on the catcher's position. This represents the calculation of the parameter g, which was introduced in the previous section. As has been shown, information about how sputtered atoms are emitted from the target's surface is necessary to determine this factor. For this reason, the detailed energy and angular distributions both of sputtered target atoms and reflected projectile ions that SDTrimSP simulations provide for a point-shaped ion beam were taken into account. In particular, a Python script was written that takes the distributions from SDTrimSP as an input and simulates the measured rate of the catcher mass change based on the results of the previous section.

The mass change rates that have to be calculated from the simulation are $y^i_{\mathrm{C,sp}}$ and $y^j_{\mathrm{C,r}}$, which were derived in equation (22) and equation (26):

$$y^i_{\mathrm{C,sp}} = y_{\mathrm{tar}} \cdot \frac{S^i}{I} \int_{A_{\mathrm{tar}}} \int_{2\pi} \Big[j\left(x,y\right) \cdot f^i_{\mathrm{sp}}\left(\Omega,x,y\right) \cdot s\left(\Omega\right) \Big] d\Omega dA$$

$$y^j_{\mathrm{C,r}} = P_{\mathrm{r}} \cdot \frac{1}{I} \int_{A_{\mathrm{tar}}} \int_0^\infty \int_{2\pi} \Big[j\left(x,y\right) \cdot f_{\mathrm{r}}\left(\Omega,E,x,y\right) \cdot y^j\left(\Omega,E\right) \cdot s\left(\Omega\right) \Big] d\Omega dE dA$$

The calculation of these mass change rates from the SDTrimSP simulation data is very similar, with the additional necessity of taking the energy of the reflected ions into account. For this reason, the following subsection will concentrate in detail on how $y^j_{\mathrm{C,r}}$ is calculated.

3.2.1 Detailed calculation of $y^j_{\mathrm{C,r}}$ and $y^i_{\mathrm{C,sp}}$

For the calculation of $y^j_{\mathrm{C,r}}$, the spatial distribution f_r, the sputtering data for the mass removal rates y^j and the reflection probability P_r are taken from SDTrimSP simulations. In contrast to the beamline setup of a fixed incoming direction of the ion beam, SDTrimSP uses a coordinate system where the target surface is defined as the xy-plane. The distributions are provided in the form of a matrix F_r, which gives the number of atoms that move away from the target at discrete polar angles θ and azimuthal angles ϕ with a discrete energy value E. For the distribution of reflected ions $f_\mathrm{r}(\Omega, E, x, y)$, the integrals over E and Ω can be rewritten by summation over the discrete energy values E, the polar angles θ and the azimuthal angles ϕ:

$$\int_0^\infty \int_{2\pi} \Big[f_\mathrm{r}(\Omega, E, x, y) \cdot y^j(\alpha_r, E) \cdot s(\Omega) \Big] d\Omega dE \approx$$

$$\approx \sum_E \sum_{\theta,\phi} \underbrace{f_\mathrm{r}(\Omega, E, x, y) \cdot \sin\theta \cdot \Delta\theta \cdot \Delta\phi \cdot \Delta E}_{\frac{1}{N_\mathrm{ions}} F_\mathrm{r}(\theta,\phi,E,x,y)} \cdot y^j(\alpha_r, E) \cdot s(\theta,\phi)$$

Here the integral over Ω was replaced by the integral over θ and ϕ using the Jacobian determinant $\sin\theta$ ($d\Omega = \sin\theta d\theta d\phi$). This discretized spatial distribution represents exactly the input from SDTrimSP, although with the normalization by division of the number of simulated ions N_ions. This is necessary due to the different normalizations of f_r and F_r with the latter describing the total number of reflected ions emitted in the direction of (θ, ϕ) with the energy E during the simulation run.

A further discretization applies for the ion-beam current density $j(x, y)$. This can be given as an input J in form of values at discrete grid points, which allows the integral to be discretized over the target area A_tar. Instead, the sum over all the grid points (x, y) where information about the current density is provided can be used:

$$y^j_{\mathrm{C,r}} \approx P_\mathrm{r} \cdot \frac{1}{I} \int_{A_\mathrm{tar}} \Big[j(x,y) \cdot \sum_E \sum_{\theta,\phi} \frac{1}{N_\mathrm{ions}} F^j_\mathrm{r}(\theta,\phi,E,x,y) \cdot y^j(\alpha_r, E) \cdot s(\theta,\phi) \Big] dA \approx$$

$$\approx P_{\mathrm{r}} \sum_{x,y} \sum_{E} \sum_{\theta,\phi} \left[\frac{1}{I} j\left(x,y\right) \cdot \Delta x \cdot \Delta y \cdot \frac{1}{N_{\mathrm{ions}}} F_{\mathrm{r}}^{j}\left(\theta,\phi,E,x,y\right) \cdot y^{j}\left(\alpha_r,E\right) \cdot s\left(\theta,\phi\right) \right] =$$

$$= P_{\mathrm{r}} \sum_{x,y} \sum_{E} \sum_{\theta,\phi} \left[\frac{J(x,y)}{I \cdot N_{\mathrm{ions}}} F_{\mathrm{r}}^{j}\left(\theta,\phi,E,x,y\right) \cdot y^{j}\left(\alpha_r,E\right) \cdot s\left(\theta,\phi\right) \right] \tag{29}$$

Here J equals exactly $j \cdot \Delta x \cdot \Delta y$ making up the final step of the discretization of $y_{\mathrm{C,r}}^{j}$. In the calculations above, the integrands were approximated to be constant over each discrete interval, which can result in an error during the calculation that is strongly dependent on how finely the respective discretizations are selected. This should be kept in mind for some simulated situations, for example, for smaller catcher distances d the exact beam profile J will heavily influence the result of the calculation requiring a fine grid of points (x,y).

One major remaining challenge is calculating the distribution of particles originating from a point (x,y) that is not the origin of the coordinate system. Shifting the origin point of the spatial distributions is easily done in carthesian coordinates, but it represents a total change of the distributions in spherical coordinates. For this reason, a variation of the point (x_H, y_H) where ions hit the target is realized by adjusting the catcher position in the calculation and thus keeping the hitting point in the origin of the coordinate system. This results in new parameters $\Delta x' = x_H \cdot \sin\alpha + \Delta x$, $d' = d - x_H \cdot \cos\alpha$ and a catcher movement in y-direction by $-y_H$. The parameters $J(x,y)$ are usually given as grid points of values where they would hit the target at $\alpha = 0$. The hit point coordinates are then easily calculated $x_H = x/\cos\alpha$, $y_H = y$ resulting in

$$\Delta x' = x \cdot \tan\alpha + \Delta x \tag{30}$$

$$d' = d - x \tag{31}$$

The remaining quantities that have not yet been adressed, the sensitivity s and the hit angle α_r, require a geometric analysis of the setup. As shown above, the point (x_C, y_C) where an atom hits the QCM is the key for taking the catcher sensitivity into account. The sensitivity of QCMs used at the IAP was found to be only dependent on the distance r_C in mm to its center point and it has a gaussian shape with $s\left(r_C\right) \propto \exp\left[-0.8707 \cdot r_C^2\right]$ (see Section 2.2.1).

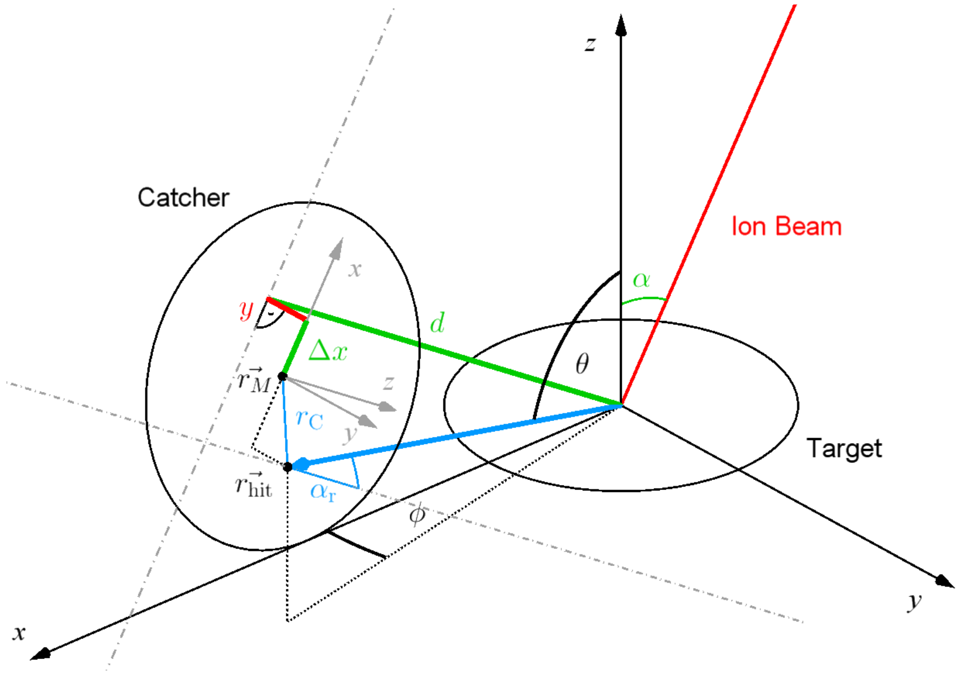

Figure 23: This sketch gives an explanation of the simulations' analysis and shows the parameters used in order to determine the number of atoms hitting the catcher.
In this coordinate system of a fixed target, the position of the catcher (center point $\vec{r_{\mathrm{M}}}$) is defined by the angle of incidence α, the distance d, the target displacement Δx and the shift y. Incoming ions (red) sputter atoms at the target, which are emitted in the direction (θ, ϕ) (blue). Under these angles, the sputtered atoms hit the plane of the catcher quartz at $\vec{r_{\mathrm{hit}}}$. The contribution of each particle is determined by the sensitivity $s(r_{\mathrm{C}})$, which is only dependent on the distance $r_{\mathrm{C}} = |\vec{r_{\mathrm{M}}} - \vec{r_{\mathrm{hit}}}|$. Additional sputtering caused by reflected ions hitting the catcher is dependent on the incident angle α_{r} on the catcher surface.

A sketch that shows how the geometric calculation was performed can be seen in Figure 23. It shows the above-mentioned SDTrimSP coordinate system, where the target lies on the xy-plane. Here the ion beam hits the target under the angle of incidence α (red line in Figure 23), which is also important to describe the catcher's position, as its surface is always parallel to the ion beam's path and the y-axis. Using the distance d between target and catcher, a possible additional displacement Δx of the target in the direction of the ion beam and a shift y, the position of the catcher can be calculated. The latter movement in y-direction is not possible in the experimental setup, but it is used in the calculation to take into account a scanned ion beam.

In order to determine the point where an emitted atom would hit the catcher, firstly, we determine the plane equation of the catcher quartz's surface. Its center point $\vec{r_M}$ and its normal vector $\vec{n}$ are given as:

$$\vec{r_M} = \begin{pmatrix} x_M \\ y_M \\ z_M \end{pmatrix} = \begin{pmatrix} d \cdot \cos(\alpha) + \Delta x \cdot \sin(\alpha) \\ y \\ d \cdot \sin(\alpha) - \Delta x \cdot \cos(\alpha) \end{pmatrix}, \qquad \vec{n} = \begin{pmatrix} \cos\alpha \\ 0 \\ \sin\alpha \end{pmatrix} \tag{32}$$

By $\vec{n} \cdot \vec{r} = \vec{n} \cdot \vec{r_M}$ this leads to the plane equation

$$x \cdot \cos\alpha + z \cdot \sin\alpha = d \tag{33}$$

A sputtered atom or a reflected ion that is emitted under angles θ and ϕ then hits the catcher at the point $\vec{r_{\text{hit}}}$:

$$\vec{r_{\text{hit}}} = r_{\text{hit}} \cdot \begin{pmatrix} \cos\phi \cdot \sin\theta \\ \sin\phi \cdot \sin\theta \\ \cos\theta \end{pmatrix} \Rightarrow r_{\text{hit}} = \frac{d}{cos\phi \cdot \sin\theta \cdot \cos\alpha + \cos\theta \cdot \sin\alpha} \tag{34}$$

Here r_{hit} was calculated by inserting the coordinates of $\vec{r_{\text{hit}}}$ into the plane equation (33). Its contribution to the catcher-QCM signal is determined by the sensitivity, so the distance $r_{\text{C}} = |\vec{r_{\text{hit}}} - \vec{r_M}|$ is important. It can easily be calculated:

$$r_{\text{C}} = \sqrt{(d \cdot \cos\alpha + \Delta x \cdot \sin\alpha - r_{\text{hit}} \cdot \cos\phi \cdot \sin\theta)^2 + (y - r_{\text{hit}} \cdot \sin\phi \cdot \sin\theta)^2 + + (d \cdot \sin\alpha - \Delta x \cdot \cos\alpha - r_{\text{hit}} \cdot \cos\theta)^2} \tag{35}$$

Finally, in order to retrieve the angle α_r under which a reflected ion hits the catcher, knowledge of $\vec{r_{\text{hit}}}$ and $\vec{n}$ are sufficient. As α_r is defined to be zero for normal incidence and the ion is reflected at the origin of the coordinate system, it is exactly the angle between these two vectors:

$$\alpha_r = \arccos\left(\frac{1}{|\vec{r_{\text{hit}}}|}\vec{r_{\text{hit}}} \cdot \vec{n}\right) \tag{36}$$

Knowledge of this angle of incidence and the energy of the reflected ion allows the calculation of its sputtering mass removal $y^j(\alpha_r, E)$. This is done by using pre-calculated SDTrimSP values for a wide variety of energy and angle combinations.

As mentioned above, most of the steps described are identical for $y^i_{\text{C,sp}}$ with the difference that sputtered atoms can be treated more easily. Due to their low kinetic energy, sputtering by these atoms hitting the catcher-QCM is ignored and their sticking is only characterized by a constant sticking coefficient S^i. For this reason, their energy and the angle under which they hit the catcher are of no concern. The quanitity $F^i_{\text{sp}}(\theta,\phi,x,y) = \sum_E F^i_{\text{sp}}(\theta,\phi,E,x,y)$ can be defined, which is the sum over all energies of the SDTrimSP input. For the mass change rate of sputtered target atoms sticking on the catcher the reflection probability P_{r} and the mass change of sputtered catcher atoms $y^j(\alpha_r, E)$ can be disregarded. Instead, the target mass removal rate y_{tar} has to be included, which can also be taken directly from an SDTrimSP simulation. Then $y^j_{\text{C,r}}$ and $y^i_{\text{C,sp}}$ can be written in similar fashion:

$$y^j_{\text{C,r}} \approx P_{\text{r}} \sum_{x,y}\sum_{E}\sum_{\theta,\phi}\left[\frac{J(x,y)}{I\cdot N_{\text{ions}}} F_{\text{r}}(\theta,\phi,E,x,y)\cdot y^j(\alpha_r,E)\cdot s(\theta,\phi)\right] \tag{37}$$

$$y^i_{\text{C,sp}} \approx y_{\text{tar}}\cdot S^i \sum_{x,y}\sum_{\theta,\phi}\left[\frac{J(x,y)}{I\cdot N_{\text{ions}}} F^i_{\text{sp}}(\theta,\phi,x,y)\cdot s(\theta,\phi)\right] \tag{38}$$

Using equation (27), the parameter g can then be calculated:

$$g = \frac{\sum_i y^i_{\text{C,sp}} - \sum_j y^j_{\text{C,r}}}{y_{\text{tar}}}$$

3.2.2 Summary

Figure 24 gives a rough recapitulation of the most important steps for calculating g that were described in the previous sections. This method is used for all simulations presented in Section 4. SDTrimSP calculations were done for the respective materials

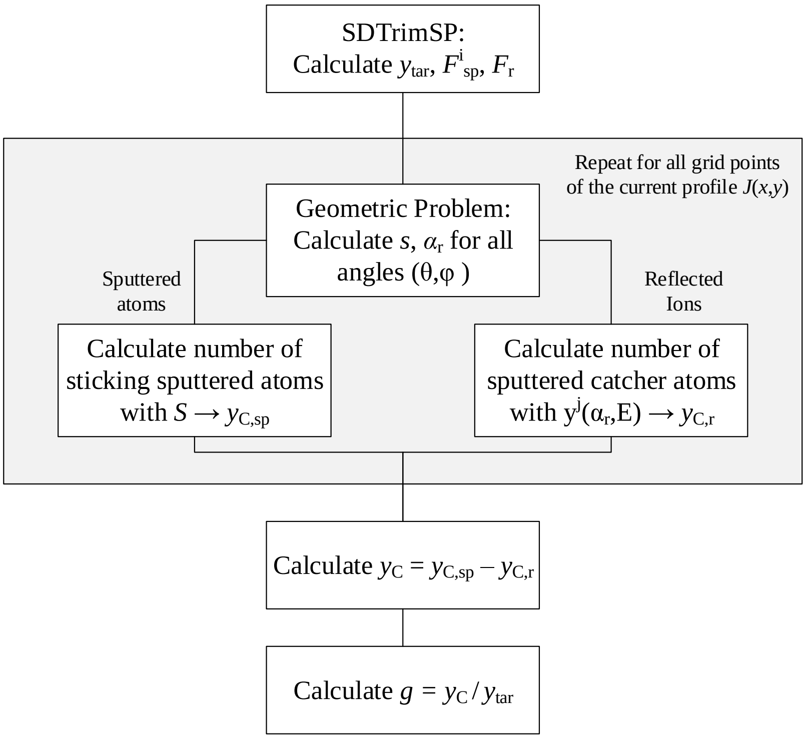

Figure 24: This schematic overview shows the steps necessary for calculating the catcher mass change y_{C} and the parameter g. Based on the data from the SDTrimSP simulation, the geometrical problem of calculating s and α_{r} has to be solved for all the grid points of the beam current profile J. Combining these results allows the calculation of $y^{i}_{\mathrm{C,sp}}$ and $y^{j}_{\mathrm{C,r}}$ and thus y_{C} and the parameter g.

and with their input the procedure for calculating the catcher signal is identical. The results of these calculations is included in the plots of the experimental results in Section 4.

As was shown in this section, several approximations were done in order to calculate g. As the experience showed, these approximations lead to errors for small catcher distances, where the results are heavily dependent on the exact beam profile. Ignoring inprecisions of SDTrimSP itself, a more sophisticated usage of numerical methods for calculating g would be an improvement at this point. However, this exceeds the scope of this thesis and will be a possible issue for future work with the catcher-QCM setup.

3.3 Simulation of Rough Surfaces with SDTrimSP-2D

3.3.1 SDTrimSP-2D

As already mentioned, the applicability of 1D simulations is limited in some cases (see section 1.2.4). For this reason, the two-dimensional expansion SDTrimSP-2D was developed at IPP, which allows the implementation of a surface structure into an SDTrimSP simulation [49]. This is achieved by expanding the geometrical description from layers to a grid, where again the cell modification is calculated from the material transport following the collision cascades. Surface cells can grow and shrink based on the transport of target atoms and thus a change in the surface morphology can be simulated. First results are very promising and can reproduce experimental observations precisely (see for an example [74]).

The surface structure can be given as a new input to SDTrimSP-2D, which can be defined with a set of (x,z)-coordinates. The initial surface of the simulated target is then created by linearly interpolating between these given points. The composition of the target can be defined with different layers that can be defined either as horizontal or as following the initial surface structure, which allows more realistic modeling, for example, of an oxide layer.

Apart from the geometrical aspects, the functionality of SDTrimSP-2D remains the same. As a result, both static and dynamic sputtering simulations are possible and the energy and angular distributions for the sputtered atoms and the reflected ions can also be calculated. The resulting output of SDTrimSP-2D can thus be used as an input for the catcher simulation in the same way as before.

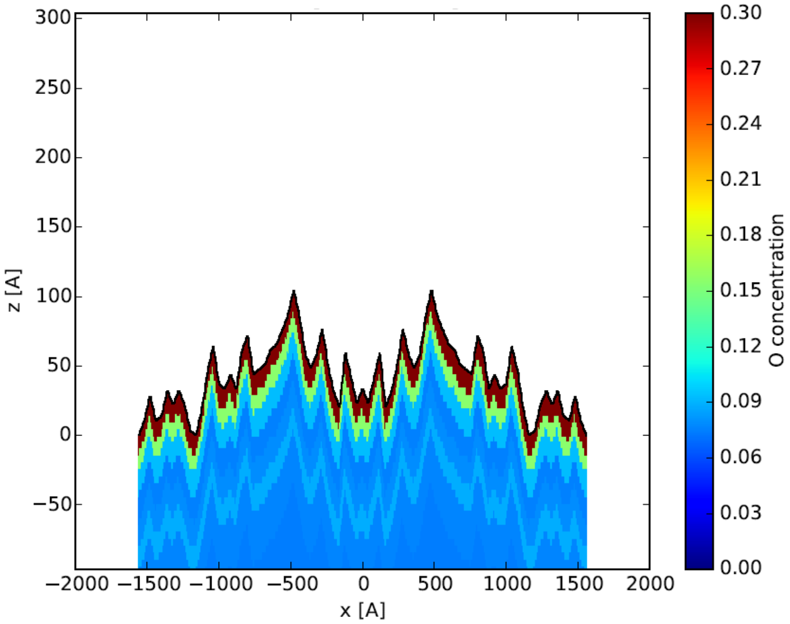

Figure 25: This graph shows the input surface for the 2D simulations created from AFM and XPS data (see Figures 15 and 17), with the color representing the O concentration in the respective area. This model has the same angle distribution and RMS value as the QCM surface analyzed, however, discrepancies due to the two-dimensional approach may still occur.

3.3.2 Approach for Fe Simulations

As was shown in Section 2.4.2, the depth-dependent composition and the surface roughness of one Fe-coated QCM were investigated. In order to correctly model the sputtering experiments of Fe samples, these aspects had to be included in the SDTrimSP-2D simulation. The composition that was retrieved from the XPS analysis was used as an input to create a target with 10 layers with different concentrations of Fe, C, N and O.

However, the 2D geometry of SDTrimSP represented an additional challenge to correctly modeling the surface structure. The AFM images in Figure 15 clearly show a structure that cannot easily be reduced to two dimensions without omitting important information about the surface. Taking one line of (x, z)-coordinates of the AFM image would, for example, result in a surface that would appear much flatter because any additional inclination in the y-direction would be ignored. For this reason, another approach was chosen by evaluating the importance of different surface aspects for sputtering. Due to the big angular dependence of the sputtering yield, the distribution of local angles plays a very important role. The initial surface structure for the 2D target was thus created in a way that it has the same angle distribution and the same RMS roughness value as the real sample. The final target surface that was used as a starting point for the Fe simulations in this thesis is shown in Figure 25, where the color denotes the O concentration.

The approach sketched in this section was used as yet unpublished work to simulate the dependence of the sputtering yield of a Fe-coated QCM on the angle of incidence and the fluence applied. The results showed a good agreement between experiment and the SDTrimSP-2D simulation, which is why this method was also chosen for simulating the catcher measurements with rough Fe targets.

4 Results and Discussion

Sputtering experiments and simulations were performed with Au, Fe and Wollastonite targets. The quantities investigated are the parameter g and the target mass removal rate y_{tar} or the target sputtering yield Y_{tar} respectively. g can be determined experimentally by measuring the mass removal rates of the target-QCM and the catcher-QCM simultaneously and dividing the two results:

$$g = \frac{y_{\mathrm{C}}}{y_{\mathrm{tar}}}$$

This is compared to the theoreticaled prediction of g based on the calculation described in the previous section.

For future experiments without a target-QCM, the reconstructed target mass removal rate y_{tar} is the most interesting quantity. It represents the estimated value for y_{tar} calculated from the experimental catcher mass change rate y_{C} and the simulated parameter g:

$$y_{\mathrm{tar}} = \frac{y_{\mathrm{C}}}{g}$$

It is determined for all the catcher measurements in the following sections and compared to the measured target mass removal rate y_{tar}.

4.1 2 keV Ar$^+$ on Au

Measurements of the sputtering yield of Au under 2 keV Ar$^+$ bombardment were performed as proof-of-principle measurements for showing the feasiblity of the catcher setup. It is a well known projectile-target combination with a wide range of comparable literature data [37]. For this reason, it is very well-suited to comparing simulated and experimental catcher yields and to investigating how well energy and angular distributions of sputtered and reflected particles can be reproduced by SDTrimSP. In order to have as few uncertainties as possible, a Au-coated catcher-QCM was used, so that the sticking factor S for sputtered Au atoms on a Au surface can be assumed to be close to one ([75], [76]).

The results of these experiments are shown in Figures 26 - 28, which were measured within the scope of this thesis and have been published already [35]. The figures show a comparison between the experimental and simulated parameter g in the left-hand plot as well as the reconstructed and measured target sputtering yield Y_{tar} on the right-hand plot respectively. Here the three defining parameters of the

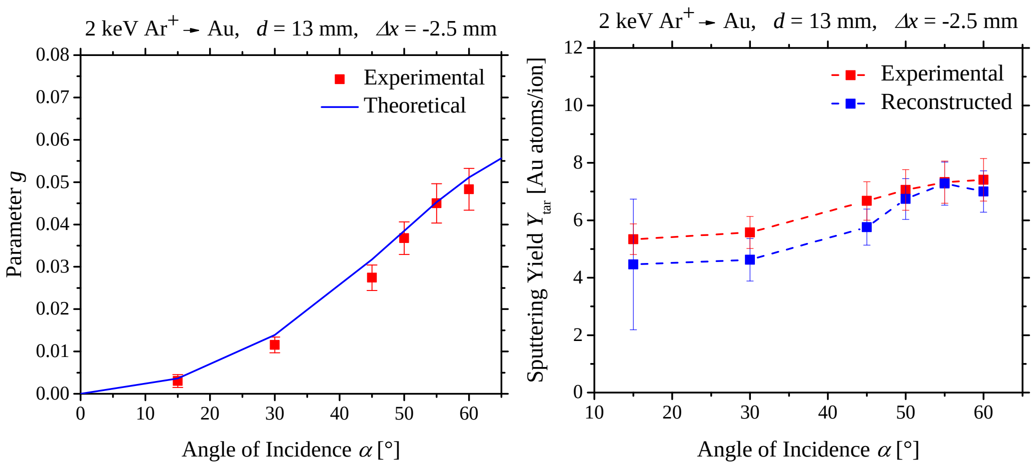

Figure 26: The experimentally measured parameter g (red in the left-hand graph) increases for higher angles of incidence α, which is supported by the simulation (blue). This can be explained by the cone of sputtered particles that is preferentially emitted normal to the target surface being only directed towards the catcher for higher incident angles. Here experiment and calculation show very good agreement. An excellent result can also be found by comparing the reconstructed target sputtering yield Y_{tar} (calculated from measured catcher yield and simulated parameter g) to the measured one, which is shown in the graph on the right.

catcher setup α, d and Δx were varied in order to find optimal positions for correct measurement signals and small deviations between experiment and simulation.

Firstly, the angle of incidence α was varied with the results being presented in Figure 26, which show a very good agreement. Sputtered Au atoms are primarily emitted in a cone around the surface normal and for small angles of incidence α they cannot reach the catcher. As the target is facing the catcher for increased angles, the amount of material hitting the catcher also increases. It can be seen that the agreement between experiment and simulation is excellent and with this data, Y_{tar} can be reconstructed very closely. Larger error bars for small angles α are caused by the small absolute values that have to be distinguished from the QCM-signal's noise and drift.

Data for different catcher distances d under a constant angle of incidence of 60 degrees, where the catcher yield is the highest, are shown in Figure 27 and these plots also show a very good agreement between experiment and simulation. For

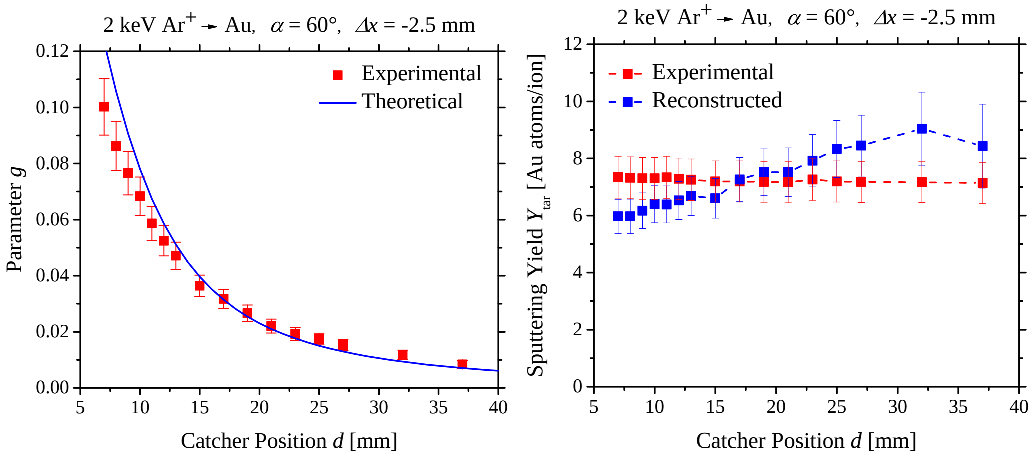

Figure 27: Very good agreement between experiment (left-hand image, red) and simulation (blue) can also be found for the parameter g for varying catcher positions d. The decrease of g can be explained by fewer sputtered particles being able to reach the sensitive catcher surface for greater distances. Small discrepancies can be found for very low distances where approximations influence the quality of the simulation. The optimal working position of d around 20 mm is also evident for the reconstructed yield Y_{tar} (right-hand graph).

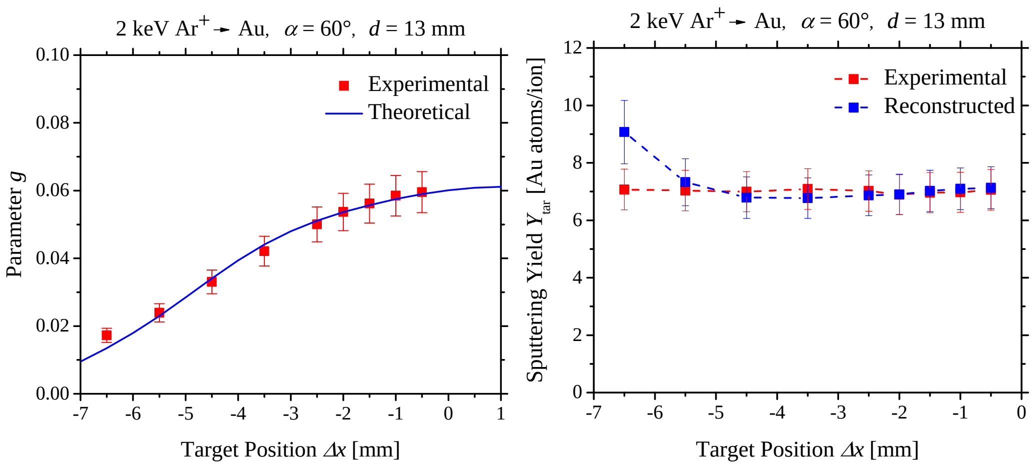

Figure 28: The variation of the target shift Δx can also be predicted very well by the simulation, showing a decrease of g for larger position changes. This is caused by fewer sputtered atoms hitting the catcher, but also an increased effect of the sputtering by reflected ions. Very good agreement can be found here for several positions for both g (graph on the left) and the reconstructed yield Y_{tar} (graph on the right).

larger distances, the parameter g follows a $1/d^2$ behavior, which can be explained by assuming that the part of the distribution of sputtered atoms registered by the catcher is small enough to be homogeneous. For closer distances, small differences are observed, which can be caused by ion beam inhomogeneities or inaccuracies in calculating the yield of the reflected ions. For larger distances, the relative error increases due to small catcher signals. As evident in the second plot of Figure 27, Y_{tar} can be reconstructed very precisely in between.

The last parameter that was changed for the catcher measurements is the target shift Δx, which due to mechanical limitations in the experimental setup at the time of the measurements could only take negative values. Again α was chosen as 60 degrees to ensure catcher signals as high as possible. For all data points obtained, the agreement here is very good and the reconstructed target yield Y_{tar} is practically identical to the measured data. For optimal positioning small Δx should be considered, as only then the cone of sputtered atoms can hit the catcher completely.

In conclusion, these proof-of-principle measurements with a Au-coated QCM can be seen as very successful. They show the preciseness of SDTrimSP predicitions for

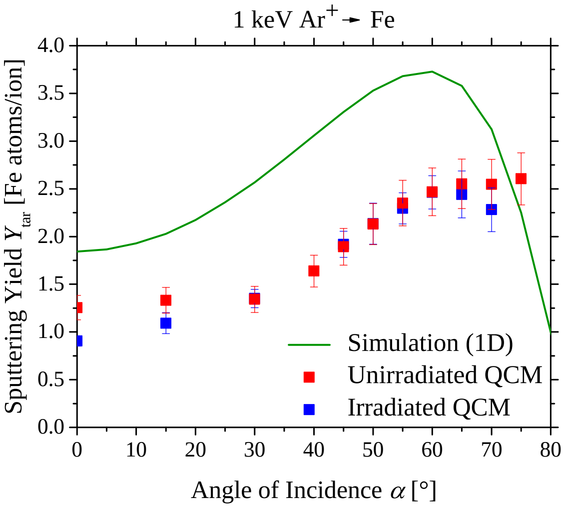

Figure 29: The target sputtering yields of the unirradiated (red) and the irradiated (blue) Fe-coated QCMs show significant differences compared to the simulation with SDTrimSP, considering both the absolute value and the angular dependence. The simulation does not include the surface roughness or a more sophisticated approach to the target composition.

the distributions of sputtered and reflected particles and thus the feasibility of using the catcher-QCM setup. A very good agreement can be reached over a wide range of catcher parameters, with only small distances d leading to deviations that can most likely be linked to the approximations done for calculating the catcher yield theoretically.

4.2 1 keV Ar^+ on Fe

As previously mentioned, the measurements with different Fe samples represent a very important method of investigating the effect of surface roughness on experiments with the catcher setup. For this reason, one QCM that had been previously irradiated with $6.7 \cdot 10^{21} \mathrm{Ar/m^2}$ under an angle of 45 degrees and an energy of 500 eV and an unirradiated QCM were chosen to be used for the experiments. The main difference of these samples would be found in the rough structure of the unirradiated sample, while the other sample should be smoothened due to the irradiation (see Figure 15). Both QCMs had been stored in an excicator at a pressure of about 1 mbar for several months before use and thus their surface composition could be assumed to be similar to the XPS composition (see Figure 17) due to oxidation during the storage.

4.2.1 Target Sputtering Yield

Both samples were irradiated with 1 keV Ar^+ under different angles of incidence in order to measure the angular dependence of the sputtering yield both on the target-QCM and on the catcher-QCM. The results for the respective targets are shown in Figure 29 along with a 1D SDTrimSP simulation with a pure Fe target. While the differences between the two experimental curves are not very significant, they are evidently not very well described by the simulation. Neither the absolute value nor the qualitative characteristic of the angular dependence can be reproduced correctly with this simulation. The similarity of the experimental yields suggests that the main reason for the discrepancy compared to the simulation can be found in the C, N and O concentrations of the sample. For this reason, the more thorough simulation approach presented in Section 3.3.2 was chosen, which takes into account both the composition and the surface roughness of the target.

The sputtering yields of the unirradiated target were simulated with the initial target surface shown in Figure 25, but with a small applied fluence $5 \cdot 10^{19}\text{Ar/m}^2$ in order to simulate the cleaning of the sample before the sputtering yield measurements. Then the angular dependence was simulated using the static mode of SDTrimSP-2D assuming that the small fluence during one measurement would only lead to a negligible change of the target. The result is shown in the graph on the left in Figure 30 where a very good agreement with the experimental values can be seen. From the simulation's results, the effective Fe sputtering yield was calculated, which represents the mass loss per ion due to sputtering of Fe, C, N and O divided by the mass of one Fe atom. Therefore, the low absolute value of the yields compared to a pure Fe simulation can be explained as mainly O is preferentially sputtered leading to a smaller mass loss. Only after longer irradiation the impurities would be depleted, leading to a steady state where mostly Fe would be sputtered. By including the surface structure and components in the calculation, the exact angular dependence can be quite well calculated with only small discrepancies around incident angles of 30 degrees. However, especially compared to the initial SDTrimSP simulations included in Figure 30 (green), a significant improvement can be found.

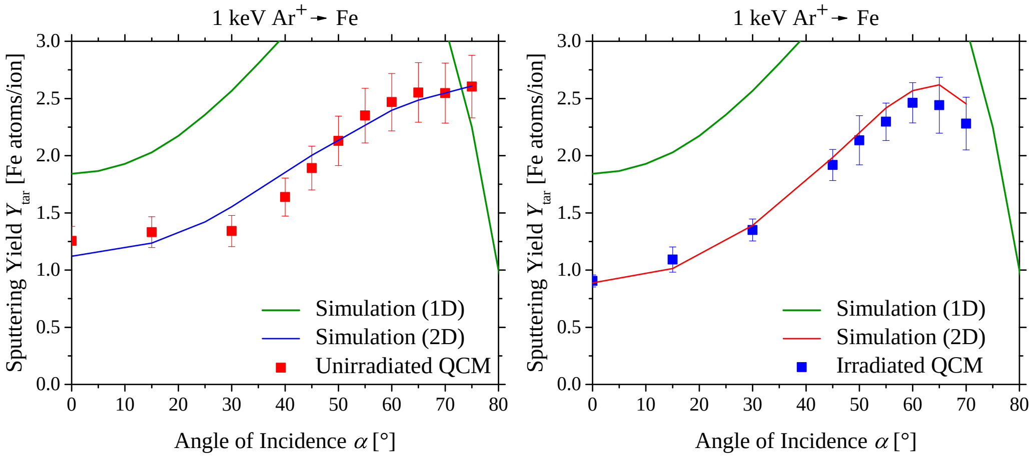

Figure 30: The graph on the left shows the angular dependence of the effective Fe sputtering yield for the unirradiated target. An SDTrimSP-2D simulation that includes surface roughness and composition (blue) fits the experimental data (red) much better than the original simulation (green). The simulation also considers a small cleaning fluence of $5 \cdot 10^{19}\text{Ar/m}^2$.
The same result can be found for reproducing the experimental yields of the irradiated target (blue) in the graph on the right, where an SDTrimSP-2D simulation (red) with a flat target and the XPS composition lead to excellent agreement after including a cleaning fluence of $3 \cdot 10^{19}\text{Ar/m}^2$ in the calculation.

Similar results can be achieved for the irradiated target, which is presented in the graph on the right in Figure 30. For the simulation with SDTrimSP-2D, a slightly different approach was chosen, as the surface roughness does not have to be taken into account here due to the smoothening process during the long-term irradiation (see section 2.4.2). Instead, a flat target with a layered composition from the XPS analysis was used for the simulation. After a small cleaning of $3 \cdot 10^{19}\mathrm{Ar/m^2}$, the angular dependence of the effective Fe sputtering yield was simulated. The results are shown as the red curve in the right-hand graph of Figure 30 with an evidently excellent agreement between experiment and simulation.

SDTrimSP-2D has thus been proven to be very well suited for explaining the target sputtering yields of the Fe samples investigated during this thesis. Discrepancies of previous simulations can mainly be attributed to the lacking description of the target composition. Large abundancies mainly of O strongly influence the sputtering behavior due to preferential sputtering of the O atoms, which leads to a smaller mass decrease and a smaller effective Fe sputtering yield. While the surface structure has been found to differ significantly, the actual sputtering yields of the smooth irradiated and rough unirradiated target only show slight discrepancies at small and large angles of incidence. As a result, the surface roughness in the low nm scale found for the targets presented hardly affects the target sputtering yield. Initial surface composition and its change by applying small cleaning fluences turn out to be much more important for a correct description of the sputtering behavior.

4.2.2 Catcher Measurements

Measurements with a Fe-coated catcher-QCM were performed in a similar fashion to the previously presented Au experiments. Figures 31 - 33 show the results both of measured and calculated parameters g as well as reconstructed sputtering yields Y_{tar} for different angles of incidence α, catcher positions d and target positions Δx. In this the results for both the flat irradiated sample and the rougher unirradiated sample are shown in order to investigate the influence of surface roughness on the catcher measurements. They also represent a possibility to determine the feasibility of using SDTrimSP-2D simulations for calculating the catcher-QCM signal. For this reason, the particle distributions necessary for catcher simulations are taken from the respective simulations shown in the previous section.

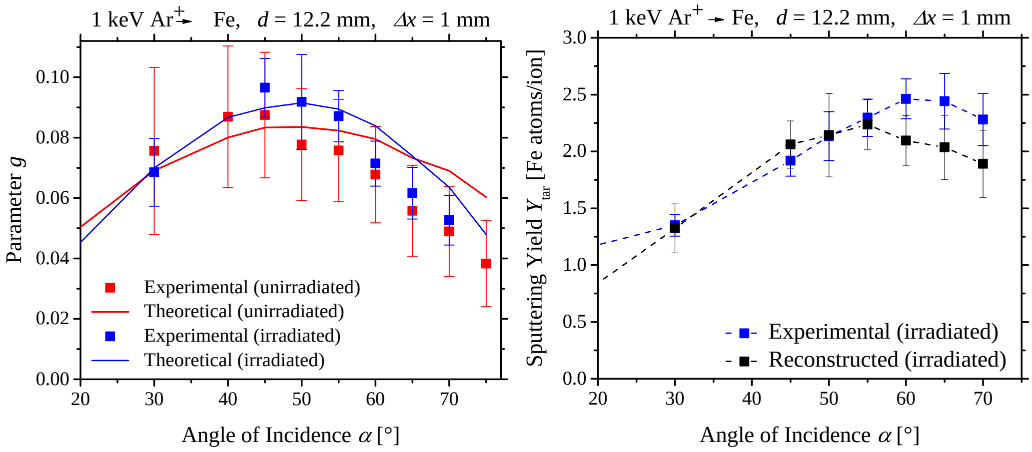

Figure 31: The angular dependence of the parameter g can be seen in the graph on the left for the unirradiated (red) and the irradiated (blue) target. The respective simulations fit the experimental results quite well, with small discrepancies at high angles α for the rough (unirradiated) target. This could be improved by using a 3D simulation that takes into account the geometry of the target in more detail.
The right-hand graph shows a comparison of the experimental (blue) and the reconstructed target sputtering yield Y_{tar} (black) for the irradiated target. The latter is too low for higher angles of incidence, but in general both curves show good agreement.

The angular dependence of the parameter g at $d = 12.2$mm and $\Delta x = 1$mm in Figure 31 on the one hand shows good agreement between experiment (squares) and simulation (lines) and on the other hand very similar values of $g\,(\alpha)$ for the rough (red) and the flat (blue) sample. The SDTrimSP-2D simulation correctly predicts the absolute value of g and its maximum at about 50 degrees. The experimental results of the irradiated target especially are very well reproduced. This can also be seen in the graph on the right, where the measured (blue) and the reconstructed target sputtering yield Y_{tar} (black) of the irradiated target are compared. For the parameter g, small discrepancies arise at higher angles for the unirradiated target, which could be explained by the simulation's limited 2D-approach for the surface roughness. It correctly takes into account the surface's distribution of angles determined by the AFM images (see section 3.3.2), but the inclinations of the simulated rough surface are always in the same plane. However, atoms are sputtered primarily around the local surface normal, which is determined by the direction of these inclinations. As a result, a more detailed calculation of the distributions for rough targets would require a 3D version of SDTrimSP that correctly takes into account the surface's geometry. Nevertheless, the 2D version also gives good results here as the small roughness in the low nm scale does not affect the sputtering behavior significantly. The experimental results show even fewer differences for rough and flat samples, which supports the previously stated conclusions that detailed information about the surface composition is much more important for a correct theoretical description of these experiments.

The variation in the catcher position d at $\alpha = 60°$ and $\Delta x = 1$mm presented in Figure 32 shows the expected $1/d^2$ behavior that is hardly affected by the different surface roughnesses. As the left-hand graph shows, the simulation very precisely reproduces the measured values of $g(d)$ as well as correctly predicting a slightly smaller value for the unirradiated sample. As a result, the reproduced target sputtering yield Y_{tar} coincides with the measured values over the whole range covered in the experiments, which is shown for the irradiated target in the graph on the right in Figure 32.

More interesting information is provided by the variation of Δx shown in Figure 33. Here larger differences for the two targets and discrepancies between experiments and simulations are observed for negative values of Δx, where the simulated values of $g(\Delta x)$ are too high. However, the differences between rough and flat sample in

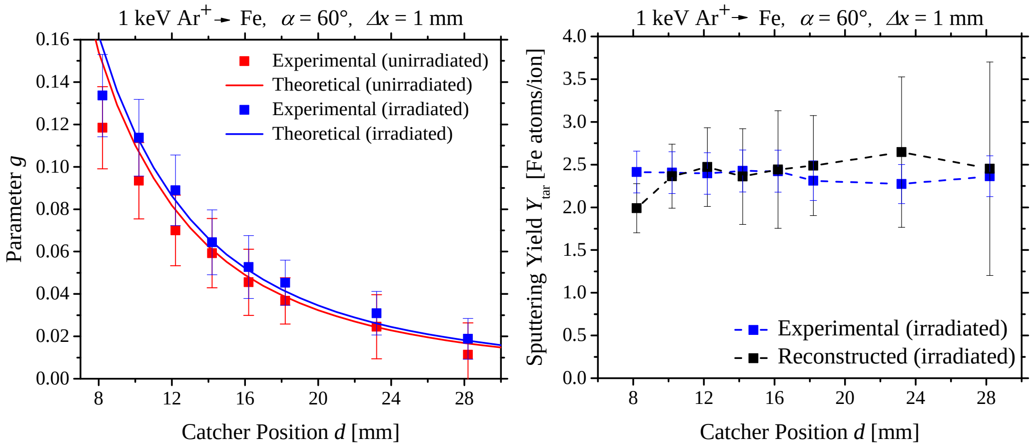

Figure 32: Both the unirradiated and the irradiated target show the $1/d^2$ behavior that has also been found with Au targets. The simulation can reproduce the measured values of g very well (graph on the left), which is also clearly seen in the excellent reproduction of Y_{tar} (graph on the right).

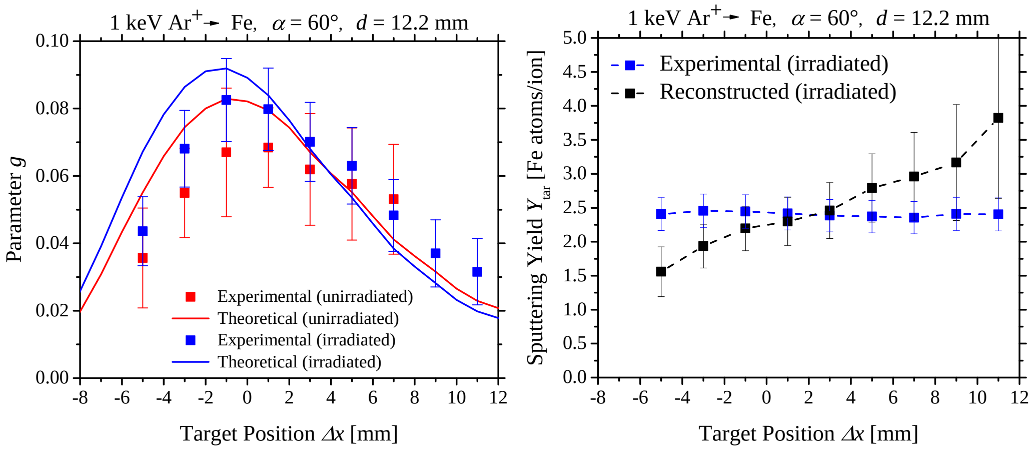

Figure 33: The Δx variation of g is described with some discrepancies between experiment and simulation for both targets, with a better agreement for positive Δx values. The lower absolute values and different maximum positions for the unirradiated target are, however, correctly predicted by the simulations.

Following the discrepancies between experimental and simulated parameter g, the reconstructed target sputtering yield Y_{tar} shows a linear increase contrary to the expected constant value.

absolute value of $g(\Delta x)$ and the sightly different positions of the maxima are well reproduced. The reconstructed target sputtering yield Y_{tar} in the right-hand graph shows a linear increase, which indicates that the data would fit together better after shifting the simulation to the right. A systematic error in determining Δx during the experiments may explain these discrepancies. This cannot be excluded, as improving the precision of determining the parameters d and Δx is one of the main concerns for future improvements in the catcher setup. However, due to the broad maximum of $g(\Delta x)$ small errors in Δx do not affect the value of g very much, as long as the working point is close to the maximum. Nevertheless, experiment and simulation in general also show good agreement for the variation of Δx and thus the simulation approach used with SDTrimSP-2D can be regarded as very well applicable for rough surfaces in the nm scale. For the unirradiated target, the simulation with a rough surface gives better theoretical results than without taking any surface structure into account. However, as previously mentioned, it should be noted that for the Fe samples used in this thesis, a precise description of the target's chemical composition represented a major improvement compared to first 1D simulations with a pure Fe target.

4.3 2 keV Ar^+ on Wollastonite ($CaSiO_3$)

Wollastonite ($CaSiO_3$) represents the first astrophysically relevant material that is investigated at IAP. Composite materials particularly represent a challenge for the catcher setup as the different sticking coefficients and possible discrepancies in the simulation due to the binding energies of the molecules make the correct interpretation of the result very challenging.

4.3.1 Target Mass Removal Rate

The experiments with Wollastonite-coated QCMs in this thesis were performed with 2 keV Ar ions with the charge state 1+ so that potential effects due to the insulating properties of the target material should be negligible for the thin film target. First the angular dependence of the target mass removal rate y_{tar} was examined, with the experimental results shown as red squares in Figure 34. Furthermore, a SDTrimSP simulation is included in this graph (blue), which fits the measured data remarkably well. This simulation uses the composition information gained from the

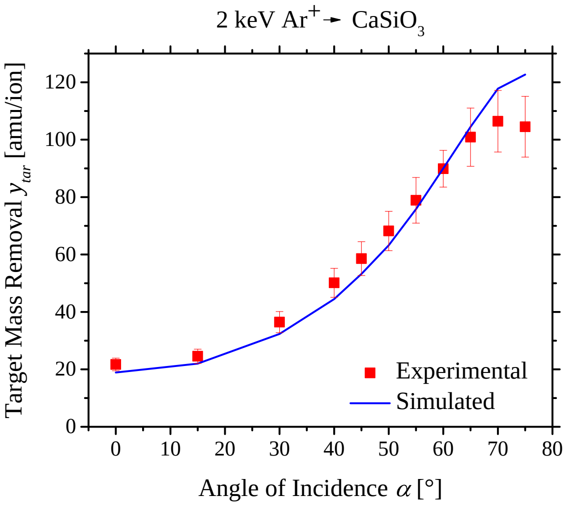

Figure 34: The mass removal rate y_{tar} of the Wollastonite target shows a very prominent angular dependence as y_{tar} increases by a factor of about 5 from 0 to 70 degrees. This behavior is predicted by both the experiment (red) and the simulation (blue), which show an excellent agreement after the composition from the XPS analysis was taken into account for the simulation.

XPS analysis and thus takes account of the significant C concentration at the surface of around 20%. The cluster-like structures observed in the AFM images of the Wollastonite samples were, however, ignored and as the sample is otherwise very smooth, these calculations could be performed with the 1D version of SDTrimSP. Both the experiment and the simulation evidently show a very large angular dependence compared to the previously investigated materials. The mass removal rate y_{tar} increases from around 20 [amu/ion] at normal incidence by a factor of more than 5 to about $110 - 120$ [amu/ion] for high angles α. As a comparison, the sputtering yield Y_{tar} of the Fe samples increased only by a factor of 2 and 2.5 and for the Au samples it is even below 1.5. According to the SDTrimSP simulation, about 50 % of the Wollastonite mass removal rate comes from preferentially sputtered O atoms and this ratio remains mostly unchanged over all the simulated angles of incidence.

As mentioned, one of the key motivations for performing space weathering-related experiments is the fact that there are hardly any experimentally derived sputtering yields available for lunar and hermean analogue materials. Hijazi et al. found a mass removal rate of 83 ± 18 [amu/ion] at an Ar^+ energy of 10 keV and under normal incidence for an anorthite material with a composition similar to Wol-

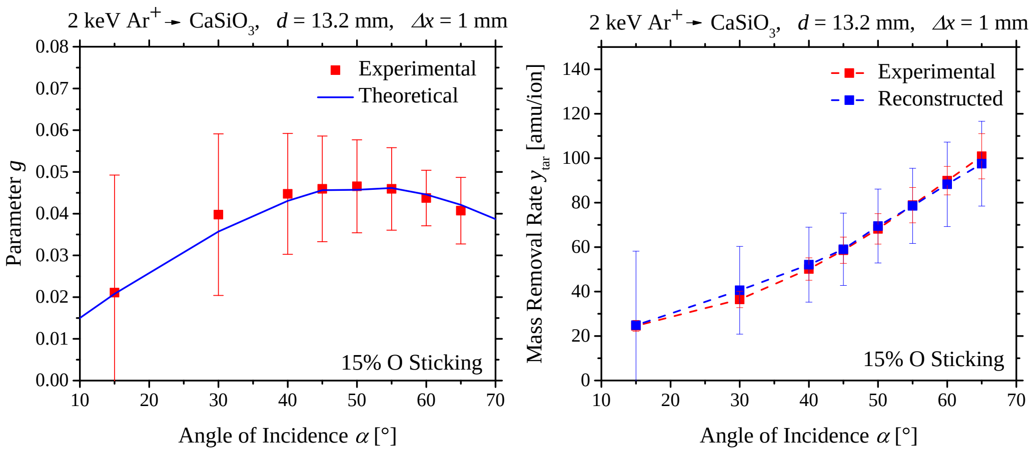

Figure 35: The graph on the left shows the parameter g under the variation of the angle of incidence α derived from experiments and simulations. The signals measured were low compared to other experiments and the agreement is very good after using the sticking coefficient of O as a fitting parameter, which leads to an assumed O sticking of 15%. The good coincidence for g also leads to a very well reconstructed target mass removal rate, which follows the experimentally measured y_{tar} very precisely.

lastonite [20]. At an energy of 10 keV the SDTrimSP simulation for Wollastonite predicts a value of about 60 [amu/ion], which would fit these results considering the differences in the target material. Nevertheless, due to the excellent agreement of experiment and simulation and the very good results achieved with SDTrimSP, these measurement results can be seen as very reliable. They also show once more how important a complete analysis of the sample is for correct simulations, as the calculated mass removal rates y_{tar} for the nominal Wollastonite composition $CaSiO_3$ showed an error of up to 50% (not included in Figure 34).

4.3.2 Catcher Measurements

During the 2 keV Ar^+ irradiations of Wollastonite, measurements with the catcher-QCM were also performed. There the three setup variables were varied in the same way as for the Au and Fe measurements in order to compare experiment and simulation and to determine how well catcher measurements are suited for working with composite materials like $CaSiO_3$.

First Figure 35 shows the results for the parameter g and the reconstructed target mass removal rate y_{tar}. The angular dependence of g is comparable to other materials, and due to low sputtering yields the signals observed in the experiment were very low, resulting in large error bars. Nevertheless, a first simulation predicts a larger signal than the experiment, which can mostly be attributed to the large amount of O sputtered from Wollastonite. Following the conclusions of other experimental work the sticking factor of O cannot be presumed to be equal to one and, due to the lack of any further information for O sticking on Wollastonite, this quantity was used as a fitting parameter for the simulated results. This leads to an assumed sticking coefficient of 0.15 for O, where the simulation fits the experiment quite well (blue line). This also leads to good agreement between the measured and reconstructed target mass removal (right-hand graph). Nevertheless, the lack of information for sticking coefficients represents a major problem for interpreting catcher results for measurements without a target-QCM, as without some additional input any rescaling becomes arbitrary. Especially for composite materials, future experiments should thus be concerned with having a method to determine or at least approximate the sticking coefficients using either experimental (for example molecular beam techniques) or theoretical (molecular dynamics simulations) methods. Otherwise an XPS analysis of the catcher-QCM after the experiment will be an indicator for the sticking of the different target materials, although how easily this data can be interpreted has yet to be ascertained.

For the variation of the catcher position d shown in Figure 36, similar conclusions as before can be taken. Again the simulated value fits the experiment after using an O sticking coefficient of 0.15 and it also shows the before observed $1/d^2$ characteristics.

However, the results of varying the target shift Δx in Figure 37 show differences between the experiment (red squares) and simulation (blue line). For $\Delta x = 1$ mm, which had been used for the other measurements, both the values coincide, but the general behavior of the curves is different. With the shape being the same, the simulated curve could be shifted to fit the experimental data, which would suggest a wrong reading of the value Δx during the measurement. This was checked after the experiment, but no systematic error was found. Due to the small changes in g for $\Delta x \approx 0$ such an error does also not affect the quality of the catcher measurements significantly and for this reason, such a position is very well suited as a working point.

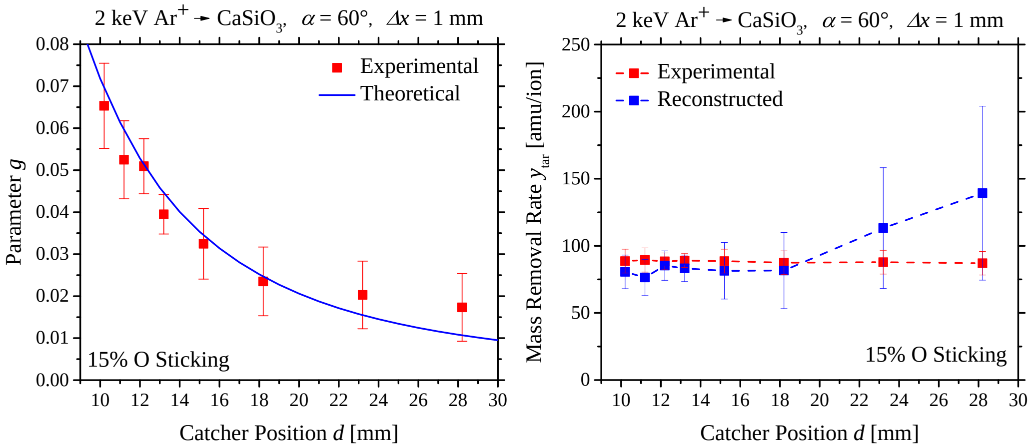

Figure 36: Comparing measured and calculated g shows that the simulation can reproduce the experiment very well for lower distances, again with an O sticking of 15%. For large distances, however, the signals become too low to realiably reconstruct the target mass removal rate, which supports the experience of previous measurements.

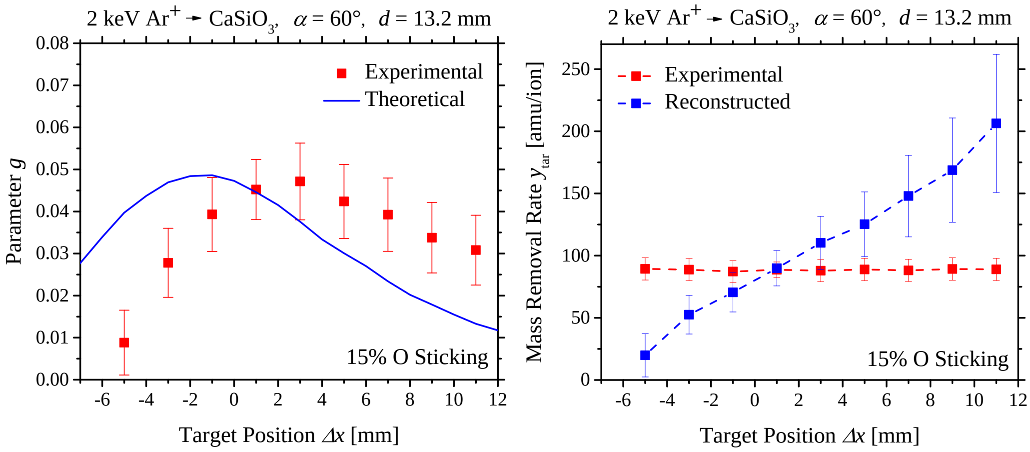

Figure 37: Despite the other two variations leading to good results, experiment and simulation differ substantially for variations of Δx. However, the fact that this does not effect the quality of the other measurements significantly shows that a low Δx represents a very stable working point. Here the sticking coefficient S of O on the catcher was also assumed to be 15% in accordance with the other Wollastonite calculations.

Nevertheless, it can not be completely disregarded, which suggests that including an additional reference for checking the correct positioning should be included in the experimental setup for future measurements. In view of the excellently fitting proof-of-principle measurements with Au targets, such an Au reference material might be feasible.

Despite these inaccuracies and the fitting of the oxygen sticking factor, experiments and simulations already show very promising results. Especially the target mass removal rate y_{tar} and the angular dependence of the parameter g were reproduced very well. As long as the target composition is known, where XPS analysis has been proven to be very useful, factors like the small cluster features observed in the AFM images and the exact chemical properties of the mineral did not have to be taken into account in the SDTrimSP simulation. This represents a very promising result as it makes measurements with composite targets like Wollastonite much easier to simulate.

5 Conclusion and Outlook

The catcher-QCM setup and its theoretical description represent a very important development for sputtering experiments at IAP. Losing the restrictions of thin film materials will open up a wide variety of possibilities for new sputtering investigations, especially for space weathering and exosphere formations. The use of stone and powder targets will allow even more realistic experiments, while still retaining the advantages of the very precise in-situ QCM technique.

The first measurements that were performed with the catcher setup as a part of this thesis showed very good results, with the simulation being able to reproduce most of the measurements very precisely. The characteristics of the parameter g are very similar for the three different sample materials investigated in the scope of this thesis. The parameter $g(\alpha)$ increases for higher angles of incidence α reaching a maximum between around 50 and 60 degrees. For the Fe and Wollastonite samples, where only elements occur with atomic masses much lower ($m_i \leq 56$) than the atomic mass of Au ($m_i = 197$), the maxima can be found at the lower end of this interval, which is connected to a much more pronounced angular dependence of the sputtering yield of lighter target materials. Variations in the catcher distance d showed a nearly identical $1/d^2$ behavior for all samples for $d \gtrsim 10\,\mathrm{mm}$. There the part of the distribution of sputtered particles that hits the catcher can be interpreted as homogeneous across the whole catcher surface, making the simulation much easier. The variation in the target shift Δx was very well reproduced for the proof-of-concept Au measurements, but proved to show some discrepancies for the Fe and Wollastonite samples. Either inaccuracies in the SDTrim simulation or systematic errors in determining Δx may be the cause, which is why additional references for checking a correct Δx are planned improvements for the future. Nevertheless, this hardly affected the quality of the other measurements, due to the broad maximum of $g(\Delta x)$ at $\Delta x \approx 0\,\mathrm{mm}$ representing a very stable working point. Other parameters for determining such a working point should be the angle of incidence α where the parameter g has its maximum around 50 - 60 degrees and a catcher distance d around 10 mm. There a high catcher signal can be achieved that is still not affected by the inaccuracies of the simulation at low d values. Smaller distances still lead to discrepancies between experiment and simulation, which are most likely connected to the approximations of the calculation and possible inhomogeneities of the ion beam profile during the experiments. However, a solution for this problem will be necessary in the future, especially considering solar-wind-related experiments. Currently, for the chosen catcher distances d between 10 and 15 mm, the maximum of g reached between 0.05 and 0.1, meaning that the catcher signals measured are only 5 - 10 % of the signals at the target-QCM using Ar ions as the projectile. The solar wind is mostly made up of protons, which will cause a much lower sputtering yield than the heavier Ar ions. In order to obtain a catcher signal that is high enough to be significantly distinguished from the catcher signal's drift and noise, lower catcher distances d may be necessary.

In general, SDTrimSP and SDTrimSP-2D proved to be very valuable tools in the simulation of the sputtering process. After taking into account the precise target composition and the surface roughness, experimental target sputtering yields could be reproduced excellently. The calculated distributions of sputtered atoms and reflected ions also allowed a very precise simulation of the catcher signal measured, even for rougher surfaces. Here the surface roughness in the low nm order only had a small effect on the sputtering behavior. Future measurements, which will be done with much rougher samples (for example, powder targets), will probably require the currently developed 3D version of SDTrimSP, which allows a complete description of the sample's geometry. Judging from the very good experiences with the previous program version so far, one can be very optimistic that the 3D version will also lead to excellent results. Another very interesting possibility for using SDTrimSP simulations is the calculation of the exosphere formation. As the calculated distributions of sputtered atoms turned out to be very reliable, these emission characteristics should be suitable for use in exosphere models. Currently these calculations are mostly based on TRIM and SRIM (see for example [26] and [27]) and the enhanced SDTrimSP program and its expansions that make it possible to simulate rough surfaces will definitely be an improvement for calculating exosphere formation.

A remaining issue for composite targets such as Wollastonite is the determination of the sticking coefficients S, especially for materials containing a large amount of O. Depositing thin target films on the catcher-QCM should lead to maximal and mostly stable sticking coefficients. On the other hand, using a Au-coated catcher-QCM would have caused a highly variable sticking coefficient as a Wollastonite layer would build up over time and change the sticking properties. Nevertheless, some reference for these coefficients should be provided either experimentally or theoretically. Molecular dynamics simulations, which exist in well-developed form for

Wollastonite, may be an easily available way to calculate the sticking. Otherwise, investigating a sample under molecular-beam evaporation represents an experimental possibility to determine sticking coefficients. An XPS analysis of the catcher-QCM after measurements have finished will also provide some information on how the sputtered atoms stick to its surface. However, there is no experience with either of these methods for determining the sticking coefficients, so the solution of this problem will be one of the major challenges for future work with the catcher setup.

Considering the successful experiments with Ar bombardment of a Wollastonite-coated QCM, the next step in astrophysically-relevant sputtering measurements will on one hand involve projectiles such as H^+ or D^+ and on the other hand replacing the target-QCM with a Wollastonite stone target. This will be the first experiment using only the catcher-QCM, which will give interesting insights into the differences from the thin film target, especially considering potential sputtering effects, and the feasibility of the catcher setup without a target-QCM. However, this will require some adaptions to the current experimental setup: the insulating properties of Wollastonite did not affect the Ar^+ measurements on the thin film with a thickness of a few 100 nm. On the other hand, a stone would charge up during ion bombardment making stable measurements impossible. For this reason, an electron flood gun that emits low energy electrons to neutralize positively charged up samples will be added to the current sample chamber setup. This will allow experiments with insulating targets, which are very important for space weathering-related research. Considering the already excellent experiences with the setup, this will lead to very exciting insights into the sputtering of lunar and hermean materials.

References

[1] Hapke B., “Space weathering from Mercury to the asteroid belt”, *Journal of Geophysical Research: Planets*, **106**, 10039 (2001)

[2] Yakshinskiy B. and Madey T., “Photon-stimulated desorption as a substantial source of sodium in the lunar atmosphere”, *Nature*, **400**, 642 (1999)

[3] Grün E., Horanyi M. and Sternovsky Z., “The lunar dust environment”, *Planetary and Space Science*, **59**, 1672 (2011)

[4] Gold T., “The lunar surface”, *Monthly Notices of the Royal Astronomical Society*, **115**, 585 (1955)

[5] Hapke B., Cohen A., Cassidy W. and Wells E., “Solar radiation effects on the optical properties of Apollo 11 samples”, *Geochimica et Cosmochimica Acta Supplement*, **1**, 2199 (1970)

[6] Conel J. and Nash D., “Spectral reflectance and albedo of Apollo 11 lunar samples: Effects of irradiation and vitrification and comparison with telescopic observations”, *Geochimica et Cosmochimica Acta Supplement*, **1**, 2013 (1970)

[7] Hapke B., Cassidy W. and Wells E., “Effects of vapor-phase deposition processes on the optical, chemical, and magnetic properties OE the lunar regolith”, *The moon*, **13**, 339 (1975)

[8] Pieters C.M., Taylor L.A., Noble S.K., Keller L.P., Hapke B., Morris R.V., Allen C.C., McKAY D.S. and Wentworth S., “Space weathering on airless bodies: Resolving a mystery with lunar samples”, *Meteoritics & Planetary Science*, **35**, 1101 (2000)

[9] Wurz P., Whitby J., Rohner U., Martín-Fernández J., Lammer H. and Kolb C., “Self-consistent modelling of Mercury’s exosphere by sputtering, micrometeorite impact and photon-stimulated desorption”, *Planetary and Space Science*, **58**, 1599 (2010)

[10] Potter A. and Morgan T., “Discovery of sodium and potassium vapor in the atmosphere of the Moon”, *Science*, **241**, 675 (1988)

[11] Vervack R.J., McClintock W.E., Killen R.M., Sprague A.L., Anderson B.J., Burger M.H., Bradley E.T., Mouawad N., Solomon S.C. and Izenberg N.R., "Mercury's complex exosphere: Results from MESSENGER's third flyby", *Science*, **329**, 672 (2010)

[12] Orsini S., Livi S., Torkar K., Barabash S., Milillo A., Wurz P., Di Lellis A., Kallio E. and the SERENA team, "SERENA: A suite of four instruments (ELENA, STROFIO, PICAM and MIPA) on board BepiColombo-MPO for particle detection in the Hermean environment", *Planetary and Space Science*, **58**, 166 (2010)

[13] Wurz P. and Lammer H., "Monte-Carlo simulation of Mercury's exosphere", *Icarus*, **164**, 1 (2003)

[14] Madey T.E., Yakshinskiy B., Ageev V. and Johnson R., "Desorption of alkali atoms and ions from oxide surfaces: Relevance to origins of Na and K in atmospheres of Mercury and the Moon", *Journal of Geophysical Research: Planets*, **103**, 5873 (1998)

[15] Borin P., Cremonese G., Marzari F., Bruno M. and Marchi S., "Statistical analysis of micrometeoroids flux on Mercury", *Astronomy & Astrophysics*, **503**, 259 (2009)

[16] Stern S.A., "The lunar atmosphere: History, status, current problems, and context", *Reviews of Geophysics*, **37**, 453 (1999)

[17] Killen R.M. and Hahn J.M., "Impact vaporization as a possible source of Mercury's calcium exosphere", *Icarus*, **250**, 230 (2015)

[18] Brueckner G. and Bartoe J.D., "Observations of high-energy jets in the corona above the quiet sun, the heating of the corona, and the acceleration of the solar wind", *The Astrophysical Journal*, **272**, 329 (1983)

[19] Feldman U., Landi E. and Schwadron N., "On the sources of fast and slow solar wind", *Journal of Geophysical Research: Space Physics*, **110** (2005)

[20] Hijazi H., Bannister M.E., Meyer H., Rouleau C.M., Barghouty A., Rickman D. and Meyer F.W., "Anorthite sputtering by H+ and Arq+ (q= 1-9) at solar

wind velocities", *Journal of Geophysical Research: Space Physics*, **119**, 8006 (2014)

[21] Bame S., Asbridge J., Feldman W., Montgomery M. and Kearney P., "Solar wind heavy ion abundances", *Solar Physics*, **43**, 463 (1975)

[22] Russell C., Luhmann J.G. and Strangeway R.J., *Space Physics: An Introduction*, Cambridge University Press (2016)

[23] Hunten D., Morgan T. and Shemansky D., *The Mercury atmosphere*, Univ. of Arizona Press Tucson (1988)

[24] Bida T.A., Killen R.M. and Morgan T.H., "Discovery of calcium in Mercury's atmosphere", *Nature*, **404**, 159 (2000)

[25] Burger M.H., Killen R.M., Vervack R.J., Bradley E.T., McClintock W.E., Sarantos M., Benna M. and Mouawad N., "Monte Carlo modeling of sodium in Mercury's exosphere during the first two MESSENGER flybys", *Icarus*, **209**, 63 (2010)

[26] Wurz P., Rohner U., Whitby J.A., Kolb C., Lammer H., Dobnikar P. and Martín-Fernández J., "The lunar exosphere: The sputtering contribution", *Icarus*, **191**, 486 (2007)

[27] Pfleger M., Lichtenegger H., Wurz P., Lammer H., Kallio E., Alho M., Mura A., McKenna-Lawlor S. and Martín-Fernández J., "3D-modeling of Mercury's solar wind sputtered surface-exosphere environment", *Planetary and space science*, **115**, 90 (2015)

[28] Ziegler J.F., Ziegler M.D. and Biersack J.P., "SRIM: The stopping and range of ions in matter (2010)", *Nuclear Instruments and Methods in Physics Research Section B: Beam Interactions with Materials and Atoms*, **268**, 1818 (2010)

[29] Hayderer G., Schmid M., Varga P., Winter H. and Aumayr F., "A highly sensitive quartz-crystal microbalance for sputtering investigations in slow ion–surface collisions", *Review of Scientific Instruments*, **70**, 3696 (1999)

[30] Hayderer G., Cernusca S., Schmid M., Varga P., Winter H., Aumayr F., Niemann D., Hoffmann V., Stolterfoht N. and Lemell C., "Kinetically assisted

potential sputtering of insulators by highly charged ions", *Physical Review Letters*, **86**, 3530 (2001)

[31] Aumayr F. and Winter H., "Potential sputtering", *Philosophical Transactions of the Royal Society of London. Series A: Mathematical, Physical and Engineering Sciences*, **362**, 77 (2004)

[32] Golczewski A., Dobes K., Wachter G., Schmid M. and Aumayr F., "A quartz-crystal-microbalance technique to investigate ion-induced erosion of fusion relevant surfaces", *Nuclear Instruments and Methods in Physics Research Section B: Beam Interactions with Materials and Atoms*, **267**, 695 (2009)

[33] Dobes K., "Erosion of Fusion Relevant Surfaces under Ion Impact", Ph.D. thesis, TU Wien (2014)

[34] Berger B.M., Stadlmayr R., Blöch D., Gruber E., Sugiyama K., Schwarz-Selinger T. and Aumayr F., "Erosion of Fe-W model system under normal and oblige D ion irradiation", *Nuclear Materials and Energy* (2017)

[35] Berger B.M., Szabo P.S., Stadlmayr R. and Aumayr F., "Sputtering measurements using a quartz crystal microbalance as a catcher", *Nuclear Instruments and Methods in Physics Research Section B: Beam Interactions with Materials and Atoms*, **406**, 533 (2017)

[36] Levinson A.A. and Taylor S.R., *Moon rocks and minerals: scientific results of the study of the Apollo 11 lunar samples with preliminary data on Apollo 12 samples*, Elsevier (2015)

[37] Behrisch R. and Eckstein W., *Sputtering by Particle Bombardment: Experiments and Computer Calculations from Threshold to MeV Energies*, Springer Science & Business Media (2007)

[38] Mutzke A., A. E., Schneider R. and Dohmen R., "SDTrimSP: Version 5.00", *IPP Report 12/8* (2011)

[39] Sigmund P., "Theory of sputtering. I. Sputtering yield of amorphous and polycrystalline targets", *Physical Review*, **184**, 383 (1969)

[40] Gruber E., "Interaction of Ions with 3D and 2D Materials", Ph.D. thesis, TU Wien (2017)

[41] Winter H. and Aumayr F., "Hollow atoms", *Journal of Physics B: Atomic, Molecular and Optical Physics*, **32**, R39 (1999)

[42] Aumayr F., Facsko S., El-Said A.S., Trautmann C. and Schleberger M., "Single ion induced surface nanostructures: a comparison between slow highly charged and swift heavy ions", *Journal of Physics: Condensed Matter*, **23**, 393001 (2011)

[43] Wilhelm R.A., El-Said A.S., Krok F., Heller R., Gruber E., Aumayr F. and Facsko S., "Highly charged ion induced nanostructures at surfaces by strong electronic excitations", *Progress in Surface Science*, **90**, 377 (2015)

[44] Jacob W. and Roth J., "Chemical sputtering", in *Sputtering by particle bombardment*, 329–400, Springer (2007)

[45] Roosendaal H.E., "Sputtering yields of single crystalline targets", in *Sputtering by particle bombardment I*, 219–256, Springer (1981)

[46] Hotston E., "Threshold energies for sputtering", *Nuclear Fusion*, **15**, 544 (1975)

[47] Küstner M., Eckstein W., Dose V. and Roth J., "The influence of surface roughness on the angular dependence of the sputter yield", *Nuclear Instruments and Methods in Physics Research Section B: Beam Interactions with Materials and Atoms*, **145**, 320 (1998)

[48] Küstner M., Eckstein W., Hechtl E. and Roth J., "Angular dependence of the sputtering yield of rough beryllium surfaces", *Journal of Nuclear Materials*, **265**, 22 (1999)

[49] Mutzke A., Schneider R. and Bandelow G., "SDTrimSP-2D: Simulation of Particles Bombarding on a Two Dimensional Target-Version 2.0", *IPP Report 12/11* (2013)

[50] Mutzke A., Bizyukov I., Schneider R. and Davis J., "Nano-scale modification of 2D surface structures exposed to 6keV carbon ions: Experiment and modeling", *Nuclear Instruments and Methods in Physics Research Section B: Beam Interactions with Materials and Atoms*, **269**, 582 (2011)

[51] Galutschek E., "Development of a 14.5 GHz All-Permanent Magnet Multicharged ECR Ion Source for Remote Operation", Ph.D. thesis, TU Wien (2005)

[52] Galutschek E., Trassl R., Salzborn E., Aumayr F. and Winter H., "Compact 14.5 GHz all-permanent magnet ECRIS for experiments with slow multicharged ions", **58**, 395 (2007)

[53] Berger B., "Laboratory work on plasma-wall-interaction processes relevant for fusion experiments", Ph.D. thesis, TU Wien ((2017)), unpublished

[54] Lu C. and Czanderna A.W., *Applications of piezoelectric quartz crystal microbalances*, Elsevier (2012)

[55] Sauerbrey G., "Verwendung von Schwingquarzen zur Wägung dünner Schichten und zur Mikrowägung", *Zeitschrift für Physik*, **155**, 206 (1959)

[56] Stevens D. and Tiersten H., "An analysis of doubly rotated quartz resonators utilizing essentially thickness modes with transverse variation", *The Journal of the Acoustical Society of America*, **79**, 1811 (1986)

[57] Gerdin G., Stygar W. and Venneri F., "Faraday cup analysis of ion beams produced by a dense plasma focus", *Journal of Applied Physics*, **52**, 3269 (1981)

[58] Szabo P., "Development of a Beam Current Monitor", Bachelor thesis, Vienna University of Technology (2015)

[59] Vig J.R. and Ballato A., "Comments on the effects of nonuniform mass loading on a quartz crystal microbalance", *Ultrasonics, Ferroelectrics, and Frequency Control, IEEE Transactions on*, **45**, 1123 (1998)

[60] Binnig G., Quate C.F. and Gerber C., "Atomic force microscope", *Physical review letters*, **56**, 930 (1986)

[61] Blöch D., "Influence of Ion Sputtering on Iron-Tungsten Alloy Surfaces and Iron Surfaces", *Diploma Thesis, TU Wien* (2017), unpublished

[62] Watts J.F. and Wolstenholme J., *An Introduction to Surface Analysis by XPS and AES*, Wiley (2003)

[63] Deer W.A., Howie R.A. and Zussman J., *Rock-forming minerals: single-chain silicates, Volume 2A* (1997)

[64] De Aza P., Guitian F. and De Aza S., "Bioactivity of wollastonite ceramics: in vitro evaluation", *Scripta metallurgica et materialia*, **31**, 1001 (1994)

[65] Sjövall P. and Uvdal P., "Oxygen sticking on Pd (111): double precursors, corrugation and substrate temperature effects", *Chemical physics letters*, **282**, 355 (1998)

[66] Eason R., *Pulsed laser deposition of thin films: applications-led growth of functional materials*, John Wiley & Sons (2007)

[67] Blake A.J. and Clegg W., *Crystal structure analysis: principles and practice*, volume 13, Oxford University Press (2009)

[68] Fernández-Pradas J., Serra P., Morenza J. and De Aza P., "Pulsed laser deposition of pseudowollastonite coatings", *Biomaterials*, **23**, 2057 (2002)

[69] Shapiro S.M., O'Shea D.C. and Cummins H.Z., "Raman Scattering Study of the Alpha-Beta Phase Transition in Quartz", *Phys. Rev. Lett.*, **19**, 361 (1967)

[70] Morita M., Ohmi T., Hasegawa E., Kawakami M. and Ohwada M., "Growth of native oxide on a silicon surface", *Journal of Applied Physics*, **68**, 1272 (1990)

[71] Möller W., Eckstein W. and Biersack J., "Tridyn-binary collision simulation of atomic collisions and dynamic composition changes in solids", *Computer Physics Communications*, **51**, 355 (1988)

[72] Eckstein W., *Computer Simulation of Ion-Solid Interactions*, Springer Science & Business Media (2013)

[73] Hofsäss H., Zhang K. and Mutzke A., "Simulation of ion beam sputtering with SDTrimSP, TRIDYN and SRIM", *Applied Surface Science*, **310**, 134 (2014)

[74] Bizyukov I., Mutzke A., Schneider R. and Davis J., "Evolution of the 2D surface structure of a silicon pitch grating under argon ion bombardment: Experiment and modeling", *Nuclear Instruments and Methods in Physics Research Section B: Beam Interactions with Materials and Atoms*, **268**, 2631 (2010)

[75] Ikuse K., Yoshimura S., Kiuchi M., Hine K. and Hamaguchi S., "Measurement of sticking probability and sputtering yield of Au by low-energy mass selected ion beams with a quartz crystal microbalance", **106**, 012016 (2008)

[76] Bachmann L. and Shin J., "Measurement of the sticking coefficients of silver and gold in an ultrahigh vacuum", *Journal of Applied Physics*, **37**, 242 (1966)

List of Figures

1 An overview of the release processes in space weathering. 2

2 An overview of the solar-wind ions' energy spectrum. 4

3 A simulated example of a collision cascade following an ion entering a solid. 6

4 An overview of the ion-surface interaction. 7

5 Examples for sputtering yields at different energies and angles of incidence. 9

6 Energy distributions of sputtered atoms and reflected ions. 11

7 Simulated angular distribution of sputtered atoms. 12

8 Simulated angular distribution of reflected ions. 13

9 The processes that have to be taken into account for rough surfaces. . 14

10 An overview of the AUGSUTIN ion-beam facility. 18

11 An overview of the QCM technique for sputtering measurements. . . 20

12 Experimental results of the QCM's sensitivity. 21

13 A sketch of the catcher-QCM setup. 24

14 An AFM image of the Au sample. 29

15 AFM images before and after irradiation. 31

16 Angle Distributions before and after irradiation. 32

17 Element concentrations from XPS at different sputter depths. 33

18 The original Wollastonite rock sample. 35

19 AFM images of the QCM surface after PLD. 37

20 The XPS spectra for Wollastonite powder and the deposited Si wafer pieces. 38

21 TOF-SIMS results for the Wollastonite deposited QCMs. 40

22 Overview of the different effects that have to be taken into account for the calculation of the catcher yield 43

23 Explanation of the simulations' analysis 50

24 A schematic overview of the calculation of the parameter g. 53

25 The randomly created surface for SDTrimSP-2D simulations of rough targets. 55

26 Au measurements for variation of the angle of incidence α. 58

27 Au measurements for variation of the catcher distance d. 59

28 Au measurements for variation of the target shift Δx. 60

29 Comparison of the experimental and simulated Fe target sputtering yields. 61
30 Experimental sputtering yields for unirradiated and irradiated Fe targets compared to SDTrimSP-2D simulations. 63
31 The parameter g and the reconstructed Fe sputtering yield for different α. 65
32 The parameter g and the reconstructed Fe sputtering yield for different d. 67
33 The parameter g and the reconstructed Fe sputtering yield for different Δx. 67
34 The angular dependence of the mass removal rate for Wollastonite. . 69
35 The parameter g and the reconstructed mass removal rate for different α. 70
36 The parameter g and the reconstructed mass removal rate for different d. 72
37 The parameter g and the reconstructed mass removal rate for different Δx. 72

List of Tables

1 Composition of the solar wind. 3
2 Overview of the different quantities used for sputter yield calculation. 22
3 Quantitative XPS analysis for Wollastonite. 39

List of Abbreviations

amu	atomic mass unit
ECRIS	Electron Cyclotron Resonance Ion Source
eV	electronvolts
FC	Faraday Cup
GHz	gigahertz
HCI	Highly-Charged Ion
IAP	Institute of Applied Physics
IPP	Max-Planck-Institute of Plasma Physics
keV	kilo-electronvolt
MeV	mega-electronvolt
QCM	Quartz Crystal Microbalance
SDTrimSP	Static-Dynamic TRIM Sequential-Parallel
SRIM	Stopping and Range of Ions in Matter
TRIDYN	Dynamic TRIM
TRIM	Transport of Ions in Matter
UHV	ultra-high vacuum

Danksagung

Das Fertigstellen dieser Diplomarbeit ist für mich der Anlass, mich bei den Personen zu bedanken, die das alles möglich gemacht haben.

Mein größter Dank gilt meinem Betreuer Prof. Dr. Friedrich Aumayr, der mich schon 2014 als Bachelorstudenten aufgenommen und mich in die wissenschaftliche Arbeit eingeführt hat. Ich möchte dir sehr herzlich dafür danken, dass du mich in den letzten Jahren so intensiv gefördert hast und mir auch mehrere Konferenzteilnahmen, einen Studienaufenthalt in Greifswald und das Mitwirken an einer wissenschaftlichen Veröffentlichung ermöglicht hast. Dass du auf jede Frage einen wertvollen Ratschlag parat hast und dass du für deine Studenten immer eine offene Tür und ein offenes Ohr hast, ist eine wirklich große Unterstützung. Das ist für mich alles andere als selbstverständlich.

Besonders möchte ich mich auch bei Dr. Bernhard Berger bedanken, der mich seit dem Beginn meiner Bachelorarbeit unter seine Fittiche genommen hat. Deine Fähigkeit, Probleme mit einer Selbstverständlichkeit zu lösen, die mir vorher noch unbekannt war, war überaus hilfreich und ich habe gerade bei der Laborarbeit sehr viel von dir gelernt. Deine Begeisterungsfähigkeit für die verschiedensten Dinge hat es im Labor auch nie langweilig werden lassen, was ich dir hoch anrechne. Unsere beruflichen Wege haben sich mittlerweile leider getrennt, aber ich wünsche dir und deiner Familie alles Gute und viel Erfolg bei eurem nächsten Lebensabschnitt in Freistadt.

Eine wichtige Rolle spielen auch meine Kolleginnen und Kollegen der Arbeitsgruppe: Janine Schwestka, Reinhard Stadlmayr, Elisabeth Gruber, Georg Harrer, Florian Laggner, Rimpei Chiba und alle anderen, mit denen ich zusammenarbeiten durfte. Ihr habt den Alltag am Institut geprägt und es mir nicht sehr schwer gemacht, auch einmal längere Abende dort zu verbringen. Gleichzeitig konnte ich mich immer auf eure Hilfsbereitschaft verlassen und ich freue mich sehr darauf, auch in Zukunft ein Teil dieser Arbeitsgruppe sein zu dürfen.

Ein herzliches Dankeschön möchte ich auch meinen Eltern aussprechen. Es gibt mir eine große Sicherheit zu wissen, dass ihr mir in jeder Lebenslage zur Seite steht, und das bedeutet mir sehr viel.